



Measurement report: *Characterization of severe spring haze episodes and influences of long-range transport in the Seoul metropolitan area in March 2019*

Hwajin Kim^{1,2}, Qi Zhang³, Yele Sun⁴

- 5 ¹Center for Environment, Health and Welfare Research, Korea Institute of Science and Technology, Seoul, 02792, Korea
²Department of Energy and Environmental Engineering, University of Science and Technology, Daejeon, 34113, Korea
³Department of Environmental Toxicology, University of California, Davis, CA 95616, USA
⁴State Key Laboratory of Atmospheric Boundary Layer Physics and Atmospheric Chemistry, Institute of Atmospheric Physics, Chinese Academy of Sciences, Beijing 100029, China
- 10 *Correspondence to: Hwajin Kim (hjkim@kist.re.kr)

Abstract. Severe haze episodes have occurred frequently in the Seoul metropolitan area (SMA) and throughout East Asian countries, especially during winter and early spring. Although notable progress has been attained in understanding these issues, the causes of severe haze formation have not yet been fully investigated. SMA haze is especially difficult to understand because the area is impacted by both local emissions from anthropogenic and biogenic activities and emissions transported from upwind sources. Here, we investigated the emission sources and formation processes of particulate matter (PM) during three haze episodes measured in early spring of 2019, from February 22 to April 2, using a high-resolution aerosol mass spectrometer (HR-AMS).

Overall, the average concentration of nonrefractory submicron aerosol (NR-PM₁) + BC was 35.1 μg m⁻³, which was composed of 38% organics, 12% SO₄, 30% NO₃, 13% NH₄ and 5% BC. The organics had an average oxygen-to-carbon (O/C) ratio of 0.52 and an average organic mass-to-carbon (OM/OC) ratio of 1.86. Seven distinct sources of organic aerosols (OA) were identified via positive matrix factorization (PMF) analysis of the HR-AMS data: vehicle-emitted hydrocarbon-like OA (HOA), cooking OA (COA), solid fuel burning-emitted OA (SFOA) and 4 different types of oxidized secondary OA with varying oxidation degrees and temporal trends.

Of the 40 days of the measurement period, 23 were identified as haze days (daily average: > 35 μg m⁻³), during which three severe haze episodes were recorded. In particular, PM₁ concentration exceeded 100 μg m⁻³ during the first episode when an alert was issued and strict emission controls were implemented in the SMA. Our results showed that nitrate dominated during the three haze episodes and accounted for 39-43% of the PM₁ concentration on average (vs. 21-24% during the low-loading period), for which there were indications of regional transport influences. Two regional transport-influenced OOA, i.e., less oxidized OOA2 (LO-OOA2) and more oxidized OOA2 (MO-OOA2), contributed substantially to the total PM₁ during the haze period (12-14% vs. 7% during the low-loading period), as well. In contrast, HOA and COA only contributed little (4-8% vs. 4-6% during the low-loading period) to the PM₁ concentration during the haze days, indicating that local emissions were likely not the main reason for the severe haze issues. Hence, from simultaneous downwind (SMA) and upwind (Beijing)



measurements using AMS and ACSM (aerosol chemical speciation monitor) over the same period, the temporal variations in PM_{10} and each chemical species showed peak values on the order of Beijing (upwind) to the SMA for approximately two days. Furthermore, lead (Pb) derived from HR-AMS measurements was observed to increase significantly during the haze period and showed good correlations with MO-OOA2 and LO-OOA2, consistent with regional sources. Multiple linear regression model indicated that the transported regionally processed air masses contributed significantly to Pb in the SMA (31%), especially during the haze period although the local burning also important by contributing 38%. The above results suggest that regional transport of polluted air masses might have played an important role in the formation of the haze episodes in the SMA during early spring.

1 Introduction

Haze is an atmospheric phenomenon where the smoke, dust, moisture, and vapor in air decrease the visibility due to the high levels of pollutants in the atmosphere (Watson, 2002). Haze has become a major concern not only to atmospheric scientists but also to the public and governments because of its detrimental effects on visibility (Zhang et al., 2010) and human health (Ebenstein et al., 2017). Haze also influences climate change directly by absorbing and reflecting solar radiation and indirectly by modifying cloud formation and properties (IPCC, 2013; Pope III and Dockery, 2006; Pöschl, 2005).

In an effort to improve the ambient air quality, the Korean government enacted the Special Act on Seoul Metropolitan Air Quality Improvement to regulate the concentrations of key pollutants such as SO_2 , CO, NO_2 , O_3 , PM, and lead (Pb) in 2005 (MOE, 2018). However, to date, the Seoul metropolitan area (SMA) is still facing air quality problems, especially in terms of high concentrations of $PM_{2.5}$ and O_3 . $PM_{2.5}$ has been one of the primary concerns due to its detrimental impacts on human health as well as on visibility. O_3 is an important air pollutant itself and contributes to the secondary formation of $PM_{2.5}$. Owing to the growing concern on haze pollution, extensive studies have been conducted in recent years to investigate the sources and formation mechanisms of haze in Korea (Schroeder et al., 2020; Peterson et al., 2019; Kim and Zhang, 2019; Nault et al., 2018; Kim et al., 2017; Kim et al., 2018). Previous studies have shown that stagnant meteorological conditions, primary emissions, secondary formation, and regional transport are the major factors leading to the formation and evolution of severe haze episodes in Korea (Nault et al., 2018; Kim et al., 2018, 2017). For example, the severe haze pollution observed in the winter of 2015 occurred due to the accumulation of local pollutants under stagnant conditions (Kim et al., 2017). Common characteristics of the stagnant meteorological parameters, e.g., a low wind speed (WS), high humidity, and shallow boundary layer (BL), during severe haze pollution periods have been observed many times at various locations in previous studies (Quan et al., 2014; Sun et al., 2014; Zhao et al., 2013; Zheng et al., 2015). However, the severe haze pollution period observed during the spring of 2016 (the KORUR-AQ campaign) was caused by both regional transport and local accumulation. Large increases in regional species, e.g., SO_4 and low-volatile oxidized organic aerosols (OA) (LV-OOA), were observed under a strong westerly wind illustrating the regional characteristic of haze pollution, followed by the enhancement of locally generated species such as NO_3 , semi-volatile low-oxidized OA (SV-OOA) and locally generated OA (e.g., hydrocarbon-like OA (HOA), cooking-



65 generated OA (COA)), under calm winds (Kim et al., 2018; Peterson et al., 2019). These results suggest that both meteorological conditions and aerosol chemistry play important roles in haze formation and evolution. Despite previous efforts in the characterization of haze pollution, our knowledge of its sources and evolution processes is still incomplete. Hence, we still have limited understanding of the formation processes of species such as OA and NO₃ during severe haze episodes, particularly for red alert periods (the daily expected PM_{2.5} concentration exceeds 50 μg m⁻³ for more than two days based on
70 the Special Act on PM_{2.5} released in February 2019) with temporary emission controls. Therefore, a more detailed characterization of the species sources and formation processes is of great importance for elucidating their impact on haze formation.

In March 2019, the SMA experienced several severe haze episodes, including a record-breaking haze episode over the past 10 years. The observed PM_{2.5} mass concentration exceeded the Korea National Ambient Air Quality Standard (35 μg m⁻³ for the
75 24-h average) by more than 2 times for longer than 5 days, and more than 50% of the measurement days violated the national standard released in March 2018 by the Ministry of Environmental Protection of Korea. Although studies have been conducted to investigate severe haze pollution from the perspectives of meteorology and modeling (Oh et al., 2020), the sources and evolution processes of the record-breaking haze episode in the early spring of 2019 remain unclear. Since the development of effective air pollution control policies must rely on knowledge about the sources, it is important to investigate the major
80 formation processes and emission sources that contribute to the high PM loadings. Therefore, understanding the sources, formation mechanisms, and evolution processes of haze pollution is important for air pollution control and the assessment of the health and climate impacts.

In this study, we conduct a comprehensive characterization of the aerosol particles in March in the SMA focusing on severe haze episodes. The high-resolution aerosol mass spectrometer (HR-AMS) is unique in providing properties of nonrefractory
85 submicron aerosol (NR-PM₁) species (organics, SO₄, NO₃, NH₄, and chloride) in real time at a high time resolution ranging from seconds to minutes (Canagaratna et al., 2007; Jayne et al., 2000). We deployed an HR-AMS, manufactured by Aerodyne Research Inc. (Billerica, MA, USA), in Seoul for 6 weeks (from February 22 to April 2) in 2019 to characterize the early spring time NR-PM₁ properties in this urban area. During the same period, a time-of-flight aerosol chemical speciation monitor (ACSM) was employed in Beijing to characterize the NR-PM_{2.5} species (organics, SO₄, NO₃, NH₄, and chloride). By
90 comparing the detailed information obtained from the in-situ measurements at both sites, our goal was to investigate the chemical evolution of the composition of PM₁ and OA, in terms of the upwind aerosol properties, and the relationship between meteorological conditions and haze formation in detail. In particular, the regional contributions to the record-breaking haze episode were investigated, which may improve our understanding of the factors and their influence on haze formation in the SMA. This information will eventually allow for the design of better pollution abatement strategies and red alert control
95 measures. Here, we report (1) the general mass concentration, chemical composition, and temporal and diurnal variations in PM₁ species during the early spring; (2) the characteristics and dynamic variations in OA sources and processes through positive matrix factorization (PMF); (3) the characteristics, sources, and important factors of the PM₁ composition and

components of OA during the haze period; and (4) the impacts of regional transport on haze formation in terms of the upwind PM properties.

100 **2 Experimental methods**

2.1 Sampling site and measurement

Real-time measurements of the particle composition and size distribution were conducted at the Korea Institute of Science and Technology (KIST) located in the northeast of Seoul (37.60°N, 127.05°E), 7 km from the city center, as reported in Kim et al. (2017). Sampling was conducted on the 5th floor of one of the KIST buildings (60 m above sea level) from February 22 to
105 April 2, 2019. This is a typical urban site affected by multiple local emissions, including nearby restaurants, traffic, burning and a variety of residential sources (Kim et al., 2017). The NR-PM₁ chemical components, including SO₄, NO₃, NH₄, chloride and organics, were measured with HR-AMS instrument (Canagaratna et al., 2007; DeCarlo et al., 2006) at a time resolution of 2.5 min. At the same time, from January 21 to March 21, 2019, NR-PM_{2.5} were sampled using an ACSM at the tower branch of the Institute of Atmospheric Physics, Chinese Academy of Sciences, Beijing, and compared with SMA NR-PM₁ data to
110 investigate the regional transport impacts (Fig. 1). The sampling setup, operation, and calibration procedures of the ACSM have been described elsewhere (Xu et al., 2015; Zhao et al., 2017).

Collocated measurements during this campaign, including the black carbon (BC) mass concentration, were performed with a multiangle absorption photometer (MAAP; Thermo Fisher Scientific, Waltham, MA, USA), and the number size distribution of the aerosols with a mobility size between 20.9 and 947.5 nm were determined with a scanning mobility particle sizer (SMPS
115 3080; TSI Inc., St. Paul, MN, USA). Both instruments conducted sampling downstream of a PM_{2.5} cyclone (URG Corp., Chapel Hill, NC, USA). The hourly concentrations of the trace gases (e.g., CO, O₃, NO₂ and SO₂) measured at the Gireum site (37.61°N, 127.03°E) were acquired from the Korea Environment Cooperation (KECO) (<http://www.airkorea.or.kr>). Meteorological measurement data such as the ambient temperature, relative humidity (RH), WS and wind direction were obtained from the nearby Jungreung site (37.61°N, 127.00°E) maintained by the Korea Meteorological Administration
120 (<http://www.kma.go.kr>). The data reported in this paper are expressed in local time, which is the Korea Standard Time (KST) and is 9 h earlier than the Universal Coordinated Time (UTC). Beijing Time is 1 h earlier than KST; thus, for the comparisons, the time has been modified to KST. Detailed descriptions of the sampling sites, sampling setup, operation, and calibration procedures can be found in Kim et al. (2017).

2.2 AMS data analysis

125 2.2.1 Basic HR- AMS data analysis

The HR-AMS data were processed and analyzed using the standard toolkit (SeQUential Igor data RetRiEval (SQUIRREL; version 1.57I), and PIKA (version 1.16H; available for download at [4](http://cires.colorado.edu/jimenez-</p></div><div data-bbox=)



group/ToFAMSResources/ToFSoftware/index.html)) in Igor Pro (Wavemetrics, Lake Oswego, OR, USA). Details on the data processing procedures have been described in previous studies (Aiken et al., 2008; Aiken et al., 2009; Allan et al., 2004). Briefly, using measurements of particle-free ambient air, modifications were made to the CO_2^+ ($m/z = 44$) signal and $^{15}\text{NN}^+$ at $m/z = 29$ to remove the contributions of the gas-phase CO_2 as well as to adjust the air signals. From the separate calibrations using pure NH_4NO_3 and $(\text{NH}_4)_2\text{SO}_4$ aerosols, the relative ionization efficiencies (RIEs) were determined to be 1.1, 1.12, and 3.99 for NO_3 , SO_4 and NH_4 , respectively. A composition-dependent collection efficiency (CDCE, 0.51 ± 0.03 (average $\pm 1\sigma$)) was applied to the data based on an algorithm published by Middlebrook et al. (2012).

The quantification of the NR- PM_{10} species was validated through a comparison of the total PM_{10} mass ($\text{PM}_{10} = \text{NR-PM}_{10} + \text{BC}$) and the apparent particle volume measured by the SMPS (Fig. S1a). As shown in Fig. S1a, the SMPS-measured particle volume was strongly correlated with the AMS-measured total mass ($r = 0.90$). From this strong correlation, the inter-comparison of the AMS mass and SMPS volume yielded a slope of 1.29, which was lower than the average particle density of 1.47 estimated using the measured chemical composition in this study (Zhang et al., 2005b) (Figs. 1c and S1d). Note that the average density of the OA was estimated to be 1.27 based on measured elemental ratios (Kuwata et al., 2012). The evolution pattern of the AMS total mass-based size distribution also agreed well with the volume-based size distribution from the SMPS measurements throughout the day (Fig. S1a and c). In addition, the total $\text{PM}_{10} + \text{BC}$ correlated well ($r = 0.86$) with the $\text{PM}_{2.5}$ mass measured using a beta attenuation mass monitor (Thermo FH62C14) at the Gireum site (~5 km from the KIST site), accounting for 75% of the $\text{PM}_{2.5}$ mass (Fig. S2). The AMS detection limits of the main chemical components are listed in Table S1 and are typically far lower than the observed concentrations. All the reported AMS-measured mass concentrations in this study are based on ambient conditions.

The elemental ratios between oxygen, carbon, hydrogen, and nitrogen as well as the organic mass-to-carbon (OM/OC) ratios of the OA were determined from an analysis of the W mode high-resolution mass spectroscopy (HRMS) data, following the method recently reported by Canagaratna et al. (2015). The elemental ratios calculated using the Aiken-ambient method (Aiken et al., 2008) are listed in Table S2 along with the ratios calculated using the Improved-Aiken method for the sake of comparison. Unless otherwise indicated, the O/C, H/C, and OM/OC ratios in this paper obtained from other studies have been calculated using the updated elemental analysis method (Canagaratna et al., 2015).

2.2.2 Particulate lead (Pb) analysis

Particulate lead (Pb) was measured with the HR-AMS. Because of its low-volatile properties, it is not straightforward to measure and quantify its concentration with an HR-AMS due to its refractory characteristics. In this study, the particulate Pb was measured with the HR-AMS and adopted as evidence for regional transport impacts. A detailed description of the validation and quantification of lead can be found in Salcedo et al. (2010), where Pb was measured with an AMS and quantified with the model developed by Salcedo et al. (2010).

In brief, the lead signal was recorded at an m/z value of 208 based on the most abundant lead isotope ($^{208}\text{Pb}^+$). The signals corresponding to the ions of the other main lead isotopes ($^{207}\text{Pb}^+$ and $^{206}\text{Pb}^+$) (Fig. S3), as well as to the doubly charged ions of



the three main lead isotopes ($^{208}\text{Pb}^{++}$, $^{207}\text{Pb}^{++}$ and $^{206}\text{Pb}^{++}$), were also observed (Fig. S4). No $^{204}\text{Pb}^+$ signal was detected, as expected due to its low abundance (0.027 relative to $^{208}\text{Pb}^+$) (De Laeter et al., 2003) and the limited signal-to-noise ratio of our measurements. Given the expected values of the isotopic ratios (De Laeter et al., 2003) and the linear fitting results, e.g., the slope (m) and Pearson's R (isotopic ratios of the singly and doubly charged ions of ^{207}Pb and ^{206}Pb vs. ^{208}Pb) summarized in Table S3, identification of the lead signals measured with the HR-AMS in the SMA was conducted. The total Pb signal for both the open and closed signals was calculated as the sum of the $^{208}\text{Pb}^+$, $^{207}\text{Pb}^+$, $^{206}\text{Pb}^+$, $^{208}\text{Pb}^{++}$, $^{207}\text{Pb}^{++}$ and $^{206}\text{Pb}^{++}$ signals using V mode data since they provide better expected ratios of Pb isotopes than that from W mode data, probably due to their high sensitivity. Because of the relatively low-volatile features of Pb, Pb slowly evaporates on the AMS vaporizer; thus, both the open and closed Pb signals were separately observed. Note that in general, the chopper-closed signal represents the instrument background signal, and there are no Pb sources in the AMS. Figure S5 compares the time series of both the open and closed Pb signals in the SMA. The sensitivity of the open signal was higher than that of the closed signal, and the isotopic ratios from the open V mode signal were the closest to the expected values (Table S3); thus, in this study, we report the Pb time series from the open V mode signal to explain the overall Pb trend and adopted it for the further investigations. Since both the open and closed signals are well correlated, using only the open signals does not distort the results. Salcedo et al. (2010) quantified the Pb concentration, considering the residual effect on the vaporizer, by developing a model from the observed open and closed Pb signals from the AMS; however, since the main purpose of this study was to use the temporal variations in Pb as an indicator for regional range transport of polluted air masses, this was not conducted in this study since it is beyond of the scope of the current study.

The contribution of the Pb sources was further analyzed using a multiple linear regression algorithm. The ambient Pb can be freshly emitted from burning sources or transported in aged air masses along with other unknown species. Hence, by including OA sources and (unknown) background of the OA, the linear decomposition algorithm determined the following:

$$\text{tsPb} = x_1 \times \text{tsHOA} + x_2 \times \text{tsCOA} + x_3 \times \text{tsLO-OOA1} + x_4 \times \text{tsLO-OOA2} + x_5 \times \text{tsMO-OOA1} + x_6 \times \text{tsMO-OOA2} + x_7 \times \text{tsSFOA} + \text{background}$$

where tsHOA, tsCOA, tsLO-OOA1, tsLO-OOA2, tsMO-OOA1, tsMO-OOA2, tsSFOA and background are the time series of each organic source and the sum of the unknown sources, and x1-7 indicate the contribution of each factor. Note that other unknown sources can generate a background level and discrepancies between the measured and reconstructed Pb concentrations. Additionally, the slight evaporation signal of Pb may cause uncertainties since only the open signal was considered for this calculation. However, this approach would be useful to estimate the time-dependent major sources of Pb among various volatile compounds. Since the Pb concentration is very low, the value of each factor is also low, but the relative contribution can be assessed.



2.2.3 Positive matrix factorization (PMF) analysis

The HRMS data of the OA were analyzed using PMF. The analysis was performed using the PMF2 algorithm in the robust mode (Paatero and Tapper, 1994) with the PMF Evaluation Toolkit (PET version 2.05) (Ulbrich et al., 2009), which was
195 retrieved from http://cires1.colorado.edu/jimenez-group/wiki/index.php/PMF-AMS_Analysis_Guide#PMF_Evaluation_Tool_Software. The data and error matrices were prepared according to the protocol described by Ulbrich et al. (2009) and outlined in Table 1 of Zhang et al. (2011). After these treatments, PMF was performed with a matrix consisting of 252 ions at m/z values between 12 and 120 by examining the number of factors (p) in the solution from one to nine.

200 After a careful evaluation based on the recommendations outlined in Zhang et al. (2011) including an investigation of the key diagnostic plots, mass spectral signatures, diurnal profiles, and correlations with external tracers, the seven-factor solution with $f_{\text{Peak}} = 0$ ($Q/Q_{\text{exp}} = 4.68$) was selected for further analysis because it satisfied the above criteria, with a distinct separation between the temporal and mass spectral variations in the seven factors. A summary of the key diagnostics is shown in Fig. S6 in the Supplement. The seven-factor solution was found to be very stable, as the mass fraction of each of the factors remained
205 relatively constant between f_{Peak} values of -1 and +0.3 (Fig. S6c). Figure S7 shows the mass spectra and the time series of the six- and eight-factor solutions, where factors 1-3 of the six-factor solution could be identified as secondary organic aerosols (SOAs) based on the O/C ratio, with a high fraction of m/z 44 and m/z 43. However, factor 3 of this solution revealed a mixed feature with cooking OA in both the mass spectra and time series. Moreover, factor 6 could also be attributed to fuel burning OA based on the fuel burning signature of the OA at m/z 60 and m/z 73, but, it exhibited a mixed feature with SOAs based on
210 the pronounced peak at m/z 43, indicating that more factors may be required to resolve these mixed factors. In contrast, the temporal variations in the eight-factor solution were similar to those in the seven-factor solution but exhibited indications of factor splitting. For example, two very similar time series of fuel burning-like factors (factors 5 and 6) were identified in the eight-factor solution, where the main difference was that factor 6 had a pronounced peak at m/z 60 and m/z 73 with lower O/C and higher H/C ratios than those of factor 5. Although different fuel burning types and sources are possible, we did not acquire
215 external evidence to validate the separation. Furthermore, given that accounting for only one fuel factor (i.e., the seven-factor solution) did not influence the separation between the other factors, it was not necessary to consider for a larger number of factors. Consequently, the seven-factor solution, which resolved hydrocarbon-like OA (HOA), cooking OA (COA), solid fuel burning (SFOA) and four types of SOAs (less oxidized OOA1 (LO-OOA1), less oxidized OOA2 (LO-OOA2), more oxidized OOA1 (MO-OOA1), and more oxidized OOA2 (MO-OOA2)), was chosen because it best represented the sources and
220 processes of the OA in SMA during early spring. Details on the source descriptions will be provided in section 3.2.

2.3 Back-trajectory and bivariate conditional probability function analysis

In this study, 96-h back trajectories were calculated every hour using version 4.8 of the Hybrid Single-Particle Lagrangian Integrated Trajectory (HYSPPLIT) model (Draxler, 2012; Draxler, 1997) for the sampling periods from February 22, 2019, to



225 April 2, 2019. Every trajectory was released at half of the mixing height at the KIST site (latitude: 37.60°N; longitude:
127.05°E). Note that half of the mixing height was automatically calculated by the HYSPLIT model. To identify the pollutant
characteristics in the different dominant transport patterns, cluster analysis was performed on the trajectories using HYSPLIT4,
and 3 clusters were identified according to the similarity in their spatial distributions. The average starting height for the back
trajectories over the entire study period was approximately 225 m and 691, respectively, for clusters 1, 2 and 3 (Fig. 1). In
addition, forward trajectories from Beijing were calculated separately for the haze periods to determine the direction and travel
230 time of the plumes departing from Beijing. Moreover, conditional probability function (CPF) (Kim et al., 2003) analysis was
performed to estimate the local sources and their impacts on the PM₁ composition and individual sources of the OA from PMF
analysis based on the wind direction coupled with the time series of the concentration of each species. The CPF plots represent
the probability that a specific compound or source is located in a certain wind direction, which can assist in the determination
of local point sources. The directional origin of regionally transported sources may not be consistent with the local surface
235 wind data used for the CPF plots due to the topography of the region (Heo et al., 2009; Kim et al., 2017).

3 Results and discussion

3.1 Overall characteristics

3.1.1 Temporal variations in the PM₁ composition and chemical properties

240 The overall characteristics and temporal variations in the spring PM₁ concentration from February 22 to April 2 in the SMA
are shown in Fig. S8, along with the time series of the gaseous pollutants, e.g., CO, SO₂, O_x and NO₂, and the meteorological
conditions (RH, temperature, wind direction, and WS). From February 22 to April 2, 2019, the average PM₁ concentration (= NR-PM₁ + BC) was 35.1 μg/m³, ranging from 3.85 to 129 μg/m³. On average, OA constituted the largest component of PM₁,
accounting for 38% of the total mass, followed by NO₃ (30%), SO₄ (12%), NH₄ (13%), BC (5%) and chloride (2%) (Fig. 1c).
Compared to the KORUS-AQ measurement, which occurred during late spring (May 2016), the NO₃ fraction was much higher
245 (30% vs 17%) whereas the organic fraction relatively decreased (38% vs 44%). This occurred due to the enhanced gas-to-
particle partitioning of semi-volatile species due to the lower temperature (4.7 °C vs 19 °C), and likelihood of additional NO₃
sources and/or NO₃ formation pathways, which are further examined in the following section. The poor correlations of RH vs
NO₃ (r = 0.40) and RH vs nitrogen oxidation ratio (NOR, r = 0.48) suggest that aqueous-phase processes unlikely played an
important role in inorganic formation during this period (Fig. S8). The primary organic aerosols (POAs) (= HOA + COA +
250 SFOA) and SOAs (= LO-OOA1 + LO-OOA2 + MO-OOA1 + MO-OOA2) accounted for 31% and 69%, respectively, of the
OA mass (Fig. 2, section 3.3). Due to the lower temperature, there was a burning source that was not identified during the
KORUS-AQ campaign (2016 May). Even with the extra source of the POAs, the total fraction of the primary species (BC +
POAs) was lower than that determined in the KORUS-AQ campaign (21% vs 26%), with the remainder (79%) being secondary
species (NO₃ + SO₄ + NH₄ + Chl + SOAs). This indicates that the aerosol pollution problem in the SMA during early spring



255 was more strongly influenced by secondary aerosols, although the formation process was apparently not the same as that determined by the KORUS-AQ measurements, where photochemical formation was the major process (Kim et al., 2018). Assuming that PM_1 represents approximately 80% of the $PM_{2.5}$ mass, we found that 58% of the measurement days (i.e., 23 days) violated the NIER daily $PM_{2.5}$ standard ($35 \mu\text{g}/\text{m}^3$). This was the most severe haze measurement since December 2015 when we started to measure the PM properties in the SMA with the AMS. This occurred because the mass concentration was indeed the highest, and the regulation of the daily $PM_{2.5}$ standard in Korea has changed from 50 to $35 \mu\text{g}/\text{m}^3$ since 2018. With a global standard, e.g., the WHO daily $PM_{2.5}$ standard, 70% of the days (30 days) violated the WHO daily standard ($25 \mu\text{g}/\text{m}^3$), thus indicating how significant the haze was during the measurement period. Details on the sources and processes that led to the very poor air quality are provided in section 3.3. In total, three haze episodes (Ep1, Ep2, and Ep3) were identified, as shown in Fig. S7. The haze features, e.g., the composition and meteorological conditions, are similar among the various haze episodes (Fig. S11), but the first haze episode, namely, Ep1, in particular, exhibited a consistently high PM_1 mass concentration for more than 5 days despite the red alert issued by the Korean government and the subsequent strict emission controls implemented during this period, which will be discussed in detail in section 3.3. Alternating high- and low-loading periods were observed. Hence, despite the frequently observed high PM_1 concentrations $> 100 \mu\text{g m}^{-3}$, the averaged PM_1 mass concentration over the entire period ($35.1 \mu\text{g}/\text{m}^3$) was still moderate.

270 3.2 Characteristics and source apportionment of the organic aerosols

Overall, on a mass basis, OA over the SMA during the early spring of 2019 consisted of approximately 59% carbon, 32% oxygen, 7.5% hydrogen, and 1.5% nitrogen (Fig. S12). The average carbon-normalized molecular formula of the OA was $C_{1.61}H_{1.61}O_{0.52}N_{0.02}$, yielding an average OM/OC ratio of 1.86 (Fig. 2c). The average elemental ratios, which were calculated using the updated elemental analysis method (Canagaratna et al., 2015), were within the range of the revised values observed at other urban locations (Canagaratna et al., 2015; Young et al., 2016 and the references therein), but they were more oxidized than those measured during the other periods, e.g., winter (OM/OC: 1.67) (Kim et al., 2017) and KORUS-AQ (OM/OC: 1.82) (Kim et al., 2018), in the SMA, suggesting that intensive SOA formation occurred during this study period. The moderate correlation ($r=0.60$, $0.19 \mu\text{g m}^{-3}$ ppbv) of the daytime SOA/ O_x ratio (10:00~16:00) suggests that photochemical processing was an important process of the SOA formation (Fig. 3), which is consistent with Herndon et al. (2008), where a strong correlation between OOA and O_x was observed in photochemically processed urban plumes originating from Mexico City. Hence, the average SOA/ O_x ratio ($0.19 \mu\text{g m}^{-3}$ ppbv) in the SMA observed in this study is at the high end of the ranges (0.03~0.19) observed in Mexico City and other megacities, e.g., Tokyo, Los Angeles, and Paris, in other seasons in SMA (Kim et al., 2018; Zhang et al., 2015), indicating that the photochemical SOA formation rate in the SMA was higher than that in the other megacities and other periods. This suggests that different types or different amounts of volatile organic compounds (VOCs) might influence the SOA formation rate during this period, although VOCs were not detected during this period. Note that only regional transport-influenced OOAs (i.e., LO-OOA2 and MO-OOA2; section 3.2.1) exhibited a notable correlation with O_x , suggesting that these two types of aerosols are photochemically formed SOAs. The other two OOA, namely, LO-OOA1



and MO-OOA1, did not exhibit a notable correlation (Fig. 3). This result indirectly suggests that VOCs in the regionally transported plumes influenced SOA loading during this period.

290 Upon examining the diurnal patterns of the atomic ratios among the elements in the OA, we found that the O/C and OM/OC ratios exhibited similar patterns with bimodal patterns at 11:00 and 16:00, but the pattern of the H/C ratio was different, peaking at 8:00 and 20:00 (Fig. 2a). This occurred because of the variations in the relative contributions of the POAs and SOAs. Additionally, the diurnal profile of the nitrogen-to-carbon (N/C) ratio was similar to those of the O/C and OM/OC ratios but gradually increased overnight until 10:00, indicating that both primary and secondary factors might influence the N/C ratio
295 (Fig. 2a).

3.2.1 Investigation of the sources of OA

In this study, seven distinct OA factors were identified, including three types of POA (HOA, COA, and SFOA) and four types of SOAs (LO-OOA1, LO-OOA2, MO-OOA1 and MO-OOA2). These four different types of SOAs were distinguished based on the O/C ratio, e.g., 0.59, 0.65, 0.99 and 1.11, respectively, but the features of their time series and diurnal patterns were also different (Fig. 2). The O/C ratios for the HOA, COA and SFOA were 0.1, 0.12 and 0.53, respectively. The four SOAs
300 (59%) account for the largest fraction of the OA mass, followed by the SFOA (17%), COA (15%) and HOA (9%) (Fig. 2). Briefly, the HOA showed a typical picket fence fragmentation pattern, as commonly seen in freshly emitted vehicle OA, with major peaks at m/z values of 41, 43, 55, and 57, which are mostly composed of $C_3H_5^+$, $C_3H_7^+$, $C_4H_7^+$, and $C_4H_9^+$, respectively (Fig. 2e). The HOA also exhibited strong correlations with tracer ions, i.e., $C_3H_7^+$ ($r = 0.86$), $C_4H_7^+$ ($r = 0.80$), $C_4H_9^+$ ($r = 0.92$),
305 and $C_5H_{11}^+$ ($r = 0.94$) (Fig. 2l and Table 1). The fraction of the HOA to the total PM is 3% (Fig. 1c), and the absolute concentration is $1.1 \mu\text{g m}^{-3}$, which is lower than the 2016 spring ($2.21 \mu\text{g m}^{-3}$) (Kim et al., 2018) and 2016 winter measurements ($1.92 \mu\text{g m}^{-3}$) (Kim et al., 2017). Because of the haze alert during the measurement period, vehicle emission control measures were implemented from March 2 to March 8 (Fig. 5). This might have influenced the decreased concentration of the HOA; however, further measurement and analysis would be needed to confirm the effectiveness of these control measures. However,
310 the decrease trend of the HOA suggests that the enhanced mass concentration during this measurement period is not formed by the accumulation of local sources. The average HOA/BC ratio was 0.6, which is close to that for diesel trucks (0.5) (Ban-Weiss et al., 2008) but much lower than the ratio for light-duty vehicles (1.4). This probably occurs due to the impact of BC from solid fuel burning sources (SMA, winter, 0.58) (Kim et al., 2018). Generally, the HOA/BC ratios observed in other large urban areas were close to those for light-duty vehicles when there were no other burning sources, e.g., Pittsburgh (1.41 ± 0.22)
315 (Zhang et al., 2005b), New York City (1.29) (Sun et al., 2011), and Mexico City (1.25) (Aiken et al., 2009); in contrast, the ratios in China and Korea were between those for diesel and gasoline vehicles, e.g., Xianghe, China (0.91) (Sun et al., 2016b), and the SMA in spring (1.03) (Kim et al., 2018).

A COA factor was also resolved in the SMA. The COAs were characterized by ratios between f55 and f57 of the OA and increased proportionally with increasing fractional contribution of the COA to the total OA, thereby exhibiting a V shape with
320 its two edges defined by the COA and HOA factors from several urban AMS data sets (Mohr et al., 2012) (Fig. S13).



325 Additionally, the mass spectrum of the COA determined in this study was almost identical to the spectrum of the COA determined in the winters of 2015 and 2016 at the same site (Figs. 2d and S14, respectively). Hence, the mass concentration of the COA is $\sim 2.1 \mu\text{g m}^{-3}$, which is similar to previous measurements at SMA ($1.55 \mu\text{g m}^{-3}$ during the KORUS-AQ campaign in May 2016, and $2.47 \mu\text{g m}^{-3}$ during the 2016 winter), suggesting that cooking styles remained consistent and local
330 accumulation was not the major haze source during the measurement period (Fig. S12). Note that the mass fraction of the COA in total PM_{10} is lower in this study (6%) compared to previous observations (e.g., 9% in the winter and 7% in the KORUS-AQ campaign) because of the enhanced total aerosol concentration during this period. The good correlation with the key tracer ions commonly used to justify the COA, such as $\text{C}_3\text{H}_3\text{O}^+$ ($m/z = 55$; $r = 0.78$), $\text{C}_3\text{H}_5\text{O}^+$ ($m/z = 57$; $r = 0.61$), $\text{C}_5\text{H}_8\text{O}^+$ ($m/z = 84$; $r = 0.94$), $\text{C}_6\text{H}_{10}\text{O}^+$ ($m/z = 98$; $r = 0.98$) and $\text{C}_7\text{H}_{12}\text{O}^+$ ($m/z = 112$; $r = 0.85$) (Fig. 2l and Table 1) and the diurnal pattern with a
335 dinner time peak (between $\sim 18:00$ and $19:00$) and a lunch time peak (at $\sim 12:00$), further confirm the source of the COA (Fig. 7) (Adhikary et al., 2010; Allan et al., 2010; Dall'Osto et al., 2013; Ge et al., 2012b; Hayes et al., 2013; He et al., 2004; Huang et al., 2010; Mohr et al., 2012, 2009; Sun et al., 2013; Young et al., 2016).

The SFOA were found to be another important POA source (7% of the total PM, Fig. 1c) in the SMA in March in addition to vehicle and cooking emissions. They were characterized by a mix of biomass burning and other fuel burning. The mass
335 spectrum of the SFOA showed typical features of biomass burning OA (BBOA), with dominant peaks at $m/z = 60$ and 73 and strong signals of oxygenated ions ($\text{C}_x\text{H}_y\text{O}_1^+$: 34.7% of the total SFOA signal; $\text{C}_x\text{H}_y\text{O}_2^+$: 14.5% of the total SFOA signal) (Fig. S15). However, the main peak could not be purely attributed to the SFOA as was reported by Kim et al. (2017), and this occurred because in this study, we also observed a burning-influenced SOA (LO-OOA1). The SFOA and LO-OOA1 contribute
340 32.9 and 29.7%, respectively, to the $\text{C}_2\text{H}_4\text{O}_2^+$ ($m/z = 60$) and $\text{C}_3\text{H}_5\text{O}_2^+$ ($m/z = 73$) signals (Fig. S16). The time series of the SFOA correlated with $\text{C}_2\text{H}_4\text{O}_2^+$ ($r = 0.85$) and $\text{C}_3\text{H}_5\text{O}_2^+$ ($r = 0.74$) (Table 1) as well as other biomass burning tracer species, including potassium ($r = 0.63$), the CHN family of ions such as $\text{C}_2\text{H}_5\text{N}^+$ ($r = 0.59$) and $\text{C}_3\text{H}_7\text{N}^+$ ($r = 0.70$) and BC ($r = 0.82$). However, it also exhibited a good correlation with Pb ($r = 0.60$), PAH ($r = 0.75$) and alkyl fragments ($\text{C}_n\text{H}^+_{2n+1}$ and $\text{C}_n\text{H}^+_{2n-1}$), including C_9H^+ ($r = 0.81$), which were likely emitted from other burning activities, such as fossil fuel combustion (Hu et al.,
345 2013). The scatter plots of f_{44} versus f_{60} indicate high f_{60} and low f_{44} values (i.e., toward the center of the triangular area of the biomass burning plumes) with increasing relative importance of biomass burning to the total OA (Fig. S13). The f_{44} and f_{60} values of the SFOA in this study were much higher than the values of the COA and HOA; in contrast, the f_{60} values of SFOA were somewhat lower than the previous BBOA values observed in the SMA (Kim et al., 2017), further verifying that the SFOA are influenced by the impacts of other burning activities such as pulverized coal combustion (Wang et al., 2013). Furthermore, BBOA are typically prevalent at locations where wood is used for residential heating (Crippa et al., 2013; Ge et al.,
350 2012a; Young et al., 2016); however, residential wood burning is not the main heating source in the SMA. For these reasons, this factor was indicated as part of the SFOA and not purely BBOA. Given that the polar plot of the SFOA revealed high concentrations at both low and high WSs (Fig. S17), the sources of the SFOA in the SMA likely include both local and regional burning activities. The local burning activities possibly occurred for the purposes of open and public area heating (e.g., construction areas and markets), disposal of leaves and woody trash in the city, and residential heating, which can include



355 all types of burning. The regional sources of the SFOA are possibly the open biomass burning activities in the agricultural
areas near Seoul (Heo et al., 2009) and the transport emissions from North Korea or farther away from Mongolia (Jung et al.,
2016), where biomass and coal burning is a major heating source during the cold season (Batmunkh et al., 2013; Jung et al.,
2010). Indeed, back-trajectory analysis indicated a high fraction of the SFOA in the plumes originating from the north,
including North Korea and the Mongolian area (Fig. 1d). The more oxidized features than those of the BBOA observed in the
360 SMA (O/C ratio, i.e., 0.53 vs 0.34 (Kim et al., 2017) further supports that there is some influence of regional transport (Fig.
2f).

In addition to the three POA factors, four SOAs were identified accounting for an average of 59% of the OA mass (Fig. 2b),
with LO-OOA1, LO-OOA2, MO-OOA1 and MO-OOA2 contributing 16, 14, 17 and 12%, respectively. They contained major
ion fragments representative of oxidized organics, e.g., CO_2^+ (m/z 44) and $\text{C}_2\text{H}_3\text{O}^+$ (m/z 43) (Fig. 2g-j). The MO-OOA2 (O/C
365 = 1.11; H/C = 1.32) and MO-OOA1 (O/C = 0.99; H/C = 1.56) (Fig. 2g and h) reside within the region representing aged and
highly oxidized SOAs in the triangle plot (Fig. S13), whereas the LO-OOA1 (O/C = 0.59; H/C = 1.61) and LO-OOA2 (O/C =
0.65; H/C = 1.62) (Fig. 2i and j) are characterized by a low O/C ratio (Fig. 2), residing within the region representing fresher
SOAs in the triangle plot (Fig. S13).

Both the MO-OOA2 and LO-OOA2 were identified as regional transport-influenced SOAs (RSOAs). These RSOAs were
370 identified first in the SMA. Among the two RSOAs, the mass spectrum of the MO-OOA2 is similar to the mass spectrum of
the RSOAs (Fig. 2g) determined by Sun et al. (2014) in China and of fulvic acid Zhang et al. (2005a) with an intense CO_2
peak. However, the mass spectrum of the LO-OOA2 is somewhat different from the less oxidized mass spectrum. However,
we suggest that both the MO-OOA2 and LO-OOA2 are RSOAs since the time series of both the MO-OOA2 and LO-OOA2
are notably correlated ($r = 0.72$) (Table 1 and Fig. S18), and they were characterized by a high peak during the haze episode,
375 which differed from the other two SOA factors, i.e., MO-OOA1 and LO-OOA1 (Fig. 2n and o). Compared to the clean period,
the RSOA concentration had increased by a factor of ~ 7 (Figs. 2, 5, 6 and Table 2). Both RSOAs were suitably correlated with
 NO_3 , SO_4 and CO_2 (Table 1). It should be noted that compared to the MO-OOA1 (vs NO_3 : 0.33; vs SO_4 : 0.39) and LO-OOA1
(vs NO_3 : $r = 0.52$; vs SO_4 : $r = 0.62$), NO_3 and SO_4 correlated better with the RSOAs (MO-OOA2 vs NO_3 : $r = 0.62$; MO-OOA2
vs SO_4 : $r = 0.75$; LO-OOA2 vs NO_3 : 0.89; LO-OOA2 vs SO_4 : 0.75), suggesting that the RSOAs had similar features to those
380 of NO_3 and SO_4 (Table 1). It should be noted that NO_3 and SO_4 exhibited regional transport features in this study. The diurnal
patterns are also similar to the shapes of NO_3 and SO_4 , with peaks in the early morning ($\sim 8:00$) because the high concentration
transported during the night in the upper layer influences the ground after the BL dissipates and the concentration is diluted by
the enhanced mixing height. Thereafter, at night, the decreased mixing height enhances the surface concentration (Fig. 7). The
influence of regional transport is further supported by the good correlation with Pb (MO-OOA2: $r = 0.73$; LO-OOA2: $r = 0.62$)
385 and C_9H_7 (MO-OOA2: $r = 0.49$; LO-OOA2: $r = 0.47$), which are tracers of coal combustion (Elser et al., 2016; Hu et al., 2013;
Sun et al., 2016a; Xu et al., 2016), while the SMA is not a major source region of coal combustion. Generally, most alkyl
fragment ($\text{C}_n\text{H}^+_{2n+1}$ and $\text{C}_n\text{H}^+_{2n-1}$) do not exhibit a good correlation with SOAs. Moreover, only C_9H_7 shows a moderate
correlation (Table 1). This would be possible if they occur in the same regionally transported plumes. The difference between



the two RSOAs is revealed by the mass spectra: the MO-OOA2 are more oxidized than the LO-OOA2 (O/C, 1.11 vs 0.65) and exhibit a higher N/C ratio (0.084 vs 0.017). Additionally, the MO-OOA2 had a better correlation with methane sulfonic acid (MSA)-related species (e.g., CH_2SO_2^+ ($r = 0.75$), CH_3SO_2^+ ($r = 0.73$), and CH_4SO_3^+ ($r = 0.72$)) (Table 1). Because a high N/C ratio and notable MSA formation would occur in secondary formation processes, the post-chemical processing occurring after transport might influence the different features. Conversely, the initial source would be the same but the status (e.g., particles vs precursors or the mixing and oxidation states) during transport would be different, although this remains unclear at this point. Since the impact of transport was dominant, it is likely that local processing and/or different source features were not pronounced.

Compared to the RSOAs, the two other SOA factors, namely, MO-OOA1 and LO-OOA1, exhibited different diurnal patterns, mass spectra, and time variations (Figs. 2 and 7, respectively). These two factors exhibited time-dependent features, revealing that the LO-OOA1 were enhanced during the first haze episode (March 5-8), whereas the MO-OOA1 were enhanced from March 21-23. Compared to the RSOAs, both of these factors were less correlated with the SOA tracers, such as NO_3 , SO_4 , CO_2^+ , and $\text{C}_2\text{H}_3\text{O}^+$, but still exhibited a moderate correlation (Table 1). This lower correlation might be due to the time-dependent feature of the factors, not the generally formed factor throughout the measurement period. These two factors had typical features. First, the diurnal profile of the LO-OOA1 during the overall period was mostly flat, but a slight increase was observed starting at 6:00 to $12.5 \mu\text{g m}^{-3}$ at 17:00 (Fig. 7) during the haze period (March 5-8), indicating the photochemical production of LO-OOA1 during the daytime. A decrease trend was observed at 9:00, likely due to local dilution when the mixing height was enhanced. Thus, this factor seems to be due to the locally formed SOAs during the haze episode (section 3.3.2), although the very high impacts of regional transport masked the local formation of secondary species. In contrast to the LO-OOA1, the MO-OOA1, with a pronounced time series on approximately March 23, showed a moderate correlation with biomass burning tracers such as $\text{C}_2\text{H}_4\text{O}_2^+$ ($r = 0.69$) and $\text{C}_3\text{H}_5\text{O}_2^+$ ($r = 0.65$). A moderate correlation was also exhibited with the SOA tracers, e.g., CO_2^+ ($r = 0.67$) and $\text{C}_2\text{H}_3\text{O}^+$ ($r = 0.63$), while a poor correlation occurred with NO_3 ($r = 0.33$) and SO_4 ($r = 0.39$) (Table 1), suggesting that this factor has secondary features but is influenced by burning sources. Furthermore, we also observed that the evolution of the MO-OOA1 and SFOAs appeared to be intrinsically linked. Overall, both diurnal patterns appeared similar during the high-loading period, i.e., high during the night and low during the afternoon, but a small afternoon peak of the MO-OOA1 was observed (Fig. 7). This indicates that the MO-OOA1 are the SOAs formed by the impacts of the burning activities on March 23. The similarity of these two sources is further supported by the CPF plots of the MO-OOA1 and SFOAs, revealing that the high concentrations from the northeast are unlikely to be associated with the other SOAs, mostly from the southwest (Fig. S17).



3.3 Investigation of the sources and evolution processes of the severe haze episodes

3.3.1 General description of the haze episode

420 PM_1 composition changed substantially as a function of the mass concentration throughout the measurement period (Fig. 4a). NO_3 was the most notable contributor to the PM, especially at high loadings. As PM_1+BC increased, the fractions of NO_3 , MO-OOA2, and LO-OOA2 continuously increased, while the POA fraction decreased. As discussed in the previous section, these three species (NO_3 , MO-OOA2, and LO-OOA2) were found to be all influenced by regional transport. Hence, the results shown here verify the notable role of regional impacts in the formation of haze pollution.

425 Comparing the high- and low-loading periods can indicate how the different sources and atmospheric processes influence haze pollution in more detail (Fig. 4b and c). The aerosol composition was different between the high- and low-loading periods, and the average concentrations of all aerosol components and sources of the OA were 1.7 – 8.6 times higher during the high-loading periods than those during the low-loading periods (Table 2, Figs. 4 and S11, respectively). The ratios of the PM species between the haze and clean periods varied in the order of NO_3 , NH_4 , Chl, SO_4 , and organic matter, although the organic matter
430 was contributed by a mixture of 7 different sources. Separating the organic sources, the LO-OOA2 showed the highest enhancement with a factor of 10.7, followed by NO_3 and MO-OOA2 at factors of 6.5 and 5.4, respectively (Table 2, Fig. 4b). In the previous section, these three species are all influenced by regional transport. Hence, the results shown here support the notable role of regional impacts in the formation of haze pollution.

The NO_3 enhancement during the haze period has also been previously observed (Kim et al., 2017), which occurred mainly
435 due to local accumulation under stagnant conditions. However, the latter is likely not the major/only reason for the haze in this case because of the accompanied enhancement in the ratio of the other regional sources, such as the LO-OOA2 and MO-OOA2. Their enhancements factors were 10.7 and 5.4, respectively, considerably higher than those of the local sources, e.g., the HOA and COA (Figs. 4 and S11, respectively), thereby indicating the role of regional transport in the formation of the haze episodes. The low correlation of the RH vs NO_3 ($r = 0.40$) and vs NOR ($r = 0.48$) excludes the aqueous-phase formation
440 of NO_3 during the haze period (Fig. S8). For these reasons, NO_3 enhancement could be caused by regional transport and not only by local formation, although it is not clear what the phase state of NO_3 (e.g., a precursor of NO and/or NO_3) is during transport. Since ammonium nitrate is a semi-volatile compound, it can continuously evaporate and condense on the co-emitted particles while they are transported. The back trajectories in Fig. 1 further show that the air masses originating from northern China passing over the Yellow Sea (cluster 1) showed the highest PM concentration with a high fraction of NO_3 , thus
445 supporting that a high loading is associated with the long-distance transport of air masses (Fig. 1). However, this does not mean that local sources do not play any role in haze formation. As shown in Figs. 4 and Table 2, during the haze period, the ratio of the local sources such as the HOA and COA was also enhanced. This enhancement could be because of the relatively lower concentration during the low-loading period (a high total to low ratio, Table 2), but this also indicates a local contribution to haze formation. Investigating the temporal evolution of haze in section 3.3.2 will provide a better understanding of how
450 regional transport and local accumulation influence haze formation.



It has already been found that SO_4 can be attributed to regional sources in the SMA (Kim et al., 2017, 2018), although its relative enhancement ratio during the haze periods in this study is lower than that of NO_3 . This is consistent with recent studies conducted in China (Chen et al., 2018; Fontes et al., 2017). Due to the emission control measures of coal combustion, NO_3 is becoming increasingly important in the occurrence of severe haze episodes (Xu et al., 2019). Given that the nitrate
455 enhancement was substantial during the Beijing haze periods (reaching above $400 \mu\text{g}/\text{m}^3$ during the first haze episode, Fig. 5), there might be a more notable influence of NO_3 and precursors from the upwind areas, thus more notably enhancing the NO_3 concentration in the downwind areas, i.e., in the SMA. In accordance with the current emission control policies in China, compared to NO_3 , SO_4 and SO_2 did not drastically change between the high- and low-loading periods (Figs. 4 and Table 2, respectively).

460 3.3.2 Chemical evolution of the haze episode

Figure 5 reveals that all compounds, such as NO_3 , SO_4 , NH_4 and organic compounds, attained peak values in the order of Beijing (line) to the SMA (filled) over approximately two days, thereby verifying the impacts of transport on haze formation in the SMA. The forward trajectory from Beijing during that time (Fig. S19) indicates that approximately two days are required for the Beijing plumes to arrive in the SMA, which coincides with the time gap shown in Fig. 5. The three severe haze periods
465 occurred with clean periods in between (Fig. S8), and each haze episode was categorized as S1, S2 and S3 where S1 is when Beijing haze developed, S2 is both SMA and Beijing are under haze period and S3 is after Beijing haze period although their haze features are somewhat different.

As shown in Fig. 5, for the first haze episode (EP1), during S1, when Beijing experienced a haze period, the SMA also experienced a haze period. Hence, all submicron aerosol species substantially increased, suggesting that not only regional
470 transport but also local accumulation impacted haze formation, while the local winds were moderate (1.7 m/s). If the SMA was subject to dynamic conditions, even if regional transport impact occurred, pollutants could be diluted. However, this was not the case, and therefore, the transported species were trapped, and local primary pollutants also accumulated, thereby intensifying the haze event, similar to the case observed during the KORUS-AQ campaign (Kim et al., 2018). Additionally, the regional-scale meteorology, such as that depicted in the Moderate Resolution Imaging Spectroradiometer (MODIS)
475 satellite image in Fig. S20, indicated that all East Asian countries experienced severe haze conditions that moved slowly from west to east, thereby transporting upwind regional pollutants, such as NO_3 , SO_4 , LO-OOA2, and MO-OOA2. Under regional movement, local accumulation also likely occurred. In contrast, the S2 stage is different, which is categorized as the time after the Beijing haze period had ended. Even after S1, when the Beijing PM concentration decreased, the SMA PM concentration remained high and even exceeded that in S1 (55.1 vs $74.5 \mu\text{g m}^{-3}$). Furthermore, unlike S1, the overall fractions of the regional
480 species of NO_3 (32 vs 35%), SO_4 (11 vs 16%), and RSOAs (MO-OOA2 and LO-OOA2) (12 vs 13%) were enhanced, while the POA (e.g., HOA, COA, and SFOAs) fraction considerably decreased from 15% to 7%, which implies almost no local source impact on the haze formation (Fig. 5) during that period, coinciding with the vehicle control period (March 2-8). The enhancement of the mass concentration, in addition to the concentration decrease of local sources, suggests that regional



transport likely was the major reason for the high enhancement. Approximately two days were required from Beijing to the
485 SMA. Hence, even though the haze period had ended in Beijing, it could still influence the SMA in approximately two days.
The stronger wind (2.0 vs 1.7 m/s) from the west also supports the impact of transport as well as the dilution effect on local
sources. Dry conditions inhibit the impact of local aqueous-phase formation of NO_3 . Indeed, the MODIS satellite image in
Fig. S20 shows the successive regional transport of the plumes from west to east; the haze in both Beijing and SMA during S1
arrived at the SMA during S2, while Beijing became clean after the plume left (S3). For these reasons, it appears that the
490 regional meteorology plays an important role in causing the high-PM pollution conditions in the SMA.

A similar trend was observed for the second haze episode (EP2), although no haze was observed when Beijing experienced
haze (S1); thus, a relatively short haze event was developed (Fig. 5). The main reason for this was that when the Beijing haze
event had developed, in contrast to the first haze event, a strong north wind occurred, which likely inhibited transport from
northern China as well as the accumulation of pollutants. However, the wind direction changed to the west again, and the SMA
495 haze episode occurred within 2 days after the Beijing haze episode occurred. Similar but more extreme chemical composition
change trends were observed. The observed haze event after the Beijing haze event had disappeared (S2) exhibited a lower
fraction of POAs (34% vs 10%) but a higher fraction of regional sources such as RSOAs (8% vs 12%), NO_3 (25% vs 33%),
and SO_4 (5% vs 14%) than those during S1 with the enhancement of the mass concentration from 29 to $54.9 \mu\text{g m}^{-3}$, thereby
strongly supporting the regional impacts on haze formation. Compared to the first haze event, a relatively short haze event
500 occurred without the impact of stagnant conditions on haze development.

Finally, the third haze episode (EP3) also revealed a similar trend, but an SMA-only haze period did not occur after the Beijing
haze had arrived in the SMA since the SMA and Beijing haze events occurred almost simultaneously (but haze still develops
successively from Beijing to the SMA) (Fig. 6). Additionally, immediately after the haze period in the SMA, a strong NW
wind occurred, which possibly decreased the PM concentration in the SMA. Although an SMA-only haze was not observed,
505 we can still identify the impacts of regional transport during the nonhaze period (S3). The PM concentration in Beijing started
to increase on March 17 at 12:00 when no haze was observed in the SMA (S1), while the SMA haze started to intensify starting
on March 19 (S3). A lower fraction of the POAs (27% vs 12%) and a higher fraction of regional sources, i.e., RSOAs (6% vs
13%), NO_3 (28% vs 39%), and SO_4 (7% vs 10%), than those during S1 was observed during S2 with the mass concentration
increasing from 24.0 to $68.6 \mu\text{g m}^{-3}$, suggesting regional impacts on haze formation, which is consistent with the pattern of the
510 previous EP1 and EP2 episodes. However, the winds weakened during this period, and stagnant conditions likely also impacted
haze formation, as was the case in S2 of EP1. This haze event disappeared due to the strong winds. Hence, there are no regional
impact-only haze periods, based on EP1 and EP2. In contrast, during this period, with strong winds from the north,
enhancement of the burning-related sources (SFOAs and MO-OOA1) was observed, consistent with the features of the MO-
OOA1 (section 3.2.1)



515 3.3.3 Diurnal patterns of the PM₁ composition during haze

Diurnal patterns can provide insights into aerosol sources and formation processes. Throughout the entire study period, the average daily variations in the concentration of the aerosol species revealed similar patterns among the different species, peaking at approximately 10:00 (Fig. 7). This is the influence of the more polluted plumes from the upper layer to the bottom layer as the ground temperature increased. More polluted upper layer plumes could be formed during the night by chemical
520 processes and/or transportation. However, under the similar meteorological conditions among the high- and low-loading and overall periods (Figs. 7a,b and S21,22, respectively), transportation is more likely rather than nighttime chemical formation. Thus, the enhanced peak at this time (~10:00) for all species suggests that there are notable impacts of regional transport on the PM concentration, and this strong impact masks the local formation processes. In an effort to understand the typical features of the high-loading period and the general PM formation processes, we investigated the diurnal patterns separately among the
525 different periods (overall and low- and high-loading periods) for each species and source (Fig. 7). Here, the high- and low-loading periods are selected based on Fig. S8 and are consistent with the periods described in section 3.3.2.

In the case of NO₃ (Figs. 7 and Fig. S21), during the overall period, the daily variations gradually increased overnight, peaked at 10:00, and then slowly decreased until 17:00, similar to the KORUS-AQ campaign in May 2016, although the overall background concentration was enhanced by a factor of 2 during the overall period and by a factor of 3 during the high-loading
530 period. The peak at 10:00 is attributed to the mixing-down of the secondary aerosols formed at night in the residual layer aloft, in addition to those generated via photochemical formation of the nitrate from NO_x, emitted from rush hour traffic period. The decrease trend over the afternoon likely occurs due to the evaporative loss of semi-volatile species at high air temperatures as well as the dilution effects due to the enhanced BL height in the afternoon. Given that somewhat high concentrations of O₃ (~20.0 ppb) and NO₂ (~40 ppb) were observed during the night (18:00 – 6:00), nitrate formation from N₂O₅ hydrolysis possibly
535 occurred, and a shallow mixing height possibly increased the concentration as well. Similar trends were observed among the overall and low- and high-loading periods, but their ranges are different: during the low-loading period, the concentration ranged from 2-6 μg m⁻³, whereas it ranged from 14-23 μg m⁻³ during the high-loading period. During the three different periods, due to the meteorological conditions, slightly higher RH and solar radiation levels were measured. The poor correlation of NOR with the RH (r = 0.54) excludes the possibility of the aqueous-phase processing effect on NO₃ formation during the high-
540 loading period (Fig. S9). Moreover, higher temperatures and WSs were observed during the high-loading period, and these conditions inhibited local accumulation and formation of NO₃. As discussed in section 3.3.1, this would suggest that the NO₃ enhancement during the high-loading period can more likely be attributed to regional transport than to local formation. The enhanced NO_x, O₃ and N₂O₅ levels suggest that both NO₃ and its precursors could be transported (Figs. 7 and S21, respectively). Alternatively, under similar meteorological conditions, the enhanced NOR level suggests that NO₃ itself can be
545 transported. More measurements and analyses are required to understand the nitrate phase during transport.

The diurnal trends of SO₄ are similar to those of NO₃ (Fig. 7), and similar trends but different concentration ranges were observed among the overall and low- and high-loading periods (Figs. 7 and S22). The concentration was elevated during the



nighttime, increased from the late afternoon (~16:00), peaked from approximately 9-10:00 on the following day, and then gradually decreased thereafter to a minimum value at 16:00 (Fig. 7b). The peak at 10:00 appeared to be due to a similar reason
550 as that for NO₃—down-mixing of the high SO₄ concentration in the upper residual layer formed at night. Unlike NO₃, during the high-loading period, the increase in SO₄ started earlier (13:00) than in the overall period (17:00), which appeared to be associated with the enhanced gas-to-particle partitioning of SO₂ and/or aqueous-phase processing facilitated by the relatively higher RH (Fig. 7b). Compared to the overall period ($r=0.67$), the better correlation between SOR and RH ($r=0.75$) during the high-loading period supports the possibility of an enhanced aqueous-phase reaction impact on SO₄ formation. The high SO₂
555 concentrations during the high-loading period would contribute to the formation of SO₄. Indeed, the precursor enhancement was more pronounced during the high-loading period than during the overall period, probably because strong impacts of regional transport occurred and SO₂ mostly depended on regional sources, while NO₂ depended on both local and regional sources. Due to the major impact of regional transport during the high-loading period, more notable diurnal variations were observed than those observed during the low-loading period. The differences between the high- and low-loading periods
560 probably occurred due to the higher than usual degree of transport. The enhanced background concentration of CO (Fig. 7) further supports the impacts of transport on this enhancement. The bivariate polar plots (Fig. S17) indicate that a high SO₂ concentration tended to occur under high-speed winds from the south and southeast directions, which shifted relative to the locations of the SO₂ point sources, thus suggesting that the industrial facilities located on the west and southwest outskirts of Seoul might be responsible (Fig. 1b of Kim et al., 2017). Similar trends were also observed for the regional transport features
565 of the other sources and species (e.g., NO₃, MO-OOA2, and LO-OOA2). The reason might be the geographical location since the Bukhan Mountains (to the north) block the wind, thus promote the circulation of the air masses. Similar trends were reported in a previous study (Heo et al., 2009; Kim et al., 2017).

In this study, the NO₃, SO₄ and chloride in PM₁ appeared to be fully neutralized by NH₄, indicating that the inorganic species were mainly present in the forms of NH₄NO₃, (NH₄)₂SO₄ and NH₄Cl (Fig. S23). Since NO₃ was more abundant than SO₄ and chloride (Fig. 1c), the NH₄ diurnal pattern was similar to that of NO₃. The diurnal pattern of the OA tended to be similar to
570 that of NO₃ and SO₄, (Fig. 7) showing the high concentration during night time peaking at ~10:00, but each source showed a clearly different trend. For example, the regional transport sources such as MO-OOA2 and LO-OOA2 were consistent with NO₃ and SO₄, while between the high- and low-loading periods, similar profiles were detected but with different ranges (Fig. 7). However, the locally generated and accumulated sources such as the POAs, LO-OOA1 and MO-OOA1 exhibited typical
575 features, as mentioned in section 3.2.

3.3.4 Evidence of regional transport: determination of particulate lead (Pb)

Atmospheric lead (Pb) is found in the aerosol-phase emissions from coal and wood combustion and waste incineration; thus, its source can be both local and regional (Heal et al., 2005; Kummer et al., 2009; Lough et al., 2005; Murphy et al., 2007; Reff et al., 2009). The time series and the diurnal cycle of the Pb mass concentration determined with the HR-AMS in the SMA is
580 shown in Fig. 8. As mentioned in section 2.2.2, Pb has been reported as the sum of the ion signals of Pb and its isotopes from



the V mode measurement under the chopper open condition. Periods with an elevated Pb level occur in the early morning with a maximum average concentration at approximately 9:00-10:00, while the concentration remains relatively low in the afternoon and starts to increase again from 17:00 (Fig. 8f). In general, the shape of the diurnal cycle of Pb is consistent with that of the regional transport-related species such as NO₃, SO₄, MO-OOA2, and LO-OOA2 (Fig. 7). The Pb time series in Fig. 8 shows that an increase in the Pb concentration occurred during the haze periods from 5-7 March, 11-13 March 11-13 and March 19-21, consistent with the other regional sources. The correlation further suggests that regional transport might possibly impact this enhancement since Pb exhibits an especially strong correlation for two components of the OA, namely, LO-OOA2 (r = 0.62) and MO-OOA2 (r = 0.73), influenced by regional transport (Table 1). Pb has a moderate correlation with the SFOA (r = 0.60), which is consistent with a previous study (Heo et al., 2009) that showed Pb can be emitted from burning activities in the SMA and along the outskirts of the SMA. This might also influence the background concentration of Pb. These results suggest that the Pb observed in the SMA is predominantly co-emitted with burning sources and transported with the plumes from the upwind sources.

The contribution of the Pb sources analyzed using a linear decomposition algorithm further showed that the ambient Pb can be freshly emitted from burning sources and transported in aged air masses along with other unknown species. Figure 8 reveals that a major source mixed with Pb was the SFOA (38%). The other mass fractions of the Pb-associated OA sources were MO-OOA2, LO-OOA2, and LO-OOA1. In particular, the contributions of the MO-OOA2 and LO-OOA2 were greatly enhanced during the high-Pb period, which is also consistent with the haze periods, i.e., March 5-7, March 11-12 and March 19-21, thus further supporting that haze formation was indeed impacted by regional transport.

The HOA, COA, and LO-OOA1 did not contribute to Pb. These results suggested that approximately half of the Pb-containing particles in the SMA originated from combustion sources of the OA, whereas the other half was associated with aged and transported sources of the OA.

4 Conclusions

The aerosol composition, sources, and evolution processes during the severe haze events that occurred in March 2019 were investigated with an HR-AMS. The average PM₁ + BC concentration was 35.1 µg/m³ and the total mass was dominated by organics (39%), followed by nitrate (30%) and sulfate (12%). Secondary species (i.e., NO₃⁻, SO₄²⁻, NH₄⁺, LO-OOA1, LO-OOA2, MO-OOA1 and MO-OOA2) accounted for 78% of the PM₁ total mass, with the remainder consisting of primary species (HOA, COA, SFOA and BC), suggesting secondary reactions being the significant source of PM. Cooking and fuel burning and vehicle emissions were identified as major POA sources in Seoul, contributing 41% on average to the total OA mass in this study.

Meteorological conditions and various emission sources influenced the concentration, composition and properties of the aerosol particles in the SMA. Moreover, haze episodes often occurred, and they tended to intensify over a period of 2-6 days and were interleaved with multiple relatively clean days. The haze event that occurred in March 2019 was strongly influenced



615 by regional transport. However, a very long haze period occurred from March 1-8 promoted by the combined impacts of
stagnant conditions and regional transport. The major regional transport-related species and/or sources were NO_3 , SO_4 , LO-
OOA2 and MO-OOA2, which were highly enhanced during the haze period. The temporal variations in the peak values of
these regional feature components decreased from Beijing to Korea over a period of two days, further verifying the important
role of regional transport in haze formation. Furthermore, based on Pb measurements by the AMS, enhancement Pb occurred
during the haze period, confirming the regional impacts on the haze episodes.

620 Another interesting feature in this study was the significance of NO_3 . Compared to previous studies in the SMA, NO_3 was
found to present at a higher concentration in spring 2019. The highest fraction and concentration of NO_3 were detected since
PM properties has investigated in the SMA using AMS from 2015 Dec., demonstrating the possibility of regional transport
features, generally considered a locally formed secondary species. This is consistent with recent studies conducted in China,
where NO_3 has become a more important driver of severe haze episodes due to the effective emission controls of coal
625 loading period, SO_4 and SO_2 did not considerably change during the haze period.

An extremely severe haze episode (the $\text{PM}_{1+\text{BC}}$ level exceeded $400 \mu\text{g}/\text{m}^3$) occurred in China ~ 2 days prior to the severe
haze episode in the SMA. In addition to the regional transport impacts, it appears that some influence was exerted on the
accelerated formation of species (e.g., nitrate) during the transport from the upwind to the downwind area of the SMA. Our
results indicate that the PM concentration, composition and sources in Korea are very complex and are influenced by
630 meteorological conditions and regional and long-range transport.

Data availability

Data presented in this manuscript are available upon request to the corresponding author

Author contribution

635 HK designed and conducted the measurements. YS provided data. HK and QZ analyzed the data and prepared the manuscript
with contributions from all authors

Acknowledgments

This work was supported by the Korea Institute of Science and Technology (KIST) Institutional Program (Atmospheric
Environment Research Program, Project No. 2E30111).

640



645 References

- Adhikary, B., Carmichael, G. R., Kulkarni, S., Wei, C., Tang, Y., Allura, A., Mena-Carrasco, M., Streets, D. G., Zhang, Q.,
Pierce, R. B., Al-Saadi, J. A., Emmons, L. K., Pfister, G. G., Avery, M. A., Barrick, J. D., Blake, D. R., Brune, W.
H., Cohen, R. C., Dibb, J. E., Fried, A., Heikes, B. G., Huey, L. G., Sullivan, D. W., Sachse, G. W., Shetter, R. E.,
Singh, H. B., Campos, T. L., Cantrell, C. A., Flocke, F. M., Dunlea, E. J., Jimenez, J. L., Weinheimer, A. J., Crouse,
650 J. D., Wennberg, P. O., Schauer, J. J., Stone, E. A., Jaffe, D. A., and Reidmiller, D. R.: A regional scale modeling
analysis of aerosol and trace gas distributions over the eastern Pacific during the INTEX-B field campaign, *Atmos.
Chem. Phys.*, 10, 2091–2115, <https://doi.org/10.5194/acp-10-2091-2010>, 2010.
- Aiken, A. C., Decarlo, P. F., Kroll, J. H., Worsnop, D. R., Huffman, J. A., Docherty, K. S., Ulbrich, I. M., Mohr, C., Kimmel,
J. R., Sueper, D., Sun, Y., Zhang, Q., Trimborn, A., Northway, M., Ziemann, P. J., Canagaratna, M. R., Onasch, T.
655 B., Alfarra, M. R., Prevot, A. S. H., Dommen, J., Duplissy, J., Metzger, A., Baltensperger, U., and Jimenez, J. L.:
O/C and OM/OC ratios of primary, secondary, and ambient organic aerosols with high-resolution time-of-flight
aerosol mass spectrometry, *Environmental Science & Technology*, 42, 4478–4485, [10.1021/es703009q](https://doi.org/10.1021/es703009q), 2008.
- Aiken, A. C., Salcedo, D., Cubison, M. J., Huffman, J. A., DeCarlo, P. F., Ulbrich, I. M., Docherty, K. S., Sueper, D., Kimmel,
J. R., Worsnop, D. R., Trimborn, A., Northway, M., Stone, E. A., Schauer, J. J., Volkamer, R. M., Fortner, E., de Foy,
660 B., Wang, J., Laskin, A., Shutthanandan, V., Zheng, J., Zhang, R., Gaffney, J., Marley, N. A., Paredes-Miranda, G.,
Arnott, W. P., Molina, L. T., Sosa, G., and Jimenez, J. L.: Mexico city aerosol analysis during MILAGRO using high
resolution aerosol mass spectrometry at the urban supersite (T0) – part 1: fine particle composition and organic source
apportionment, *Atmos. Chem. Phys.*, 9, 6633–6653, <https://doi.org/10.5194/acp-9-6633-2009>, 2009.
- Allan, J. D., Delia, A. E., Coe, H., Bower, K. N., Alfarra, M. R., Jimenez, J. L., Middlebrook, A. M., Drewnick, F., Onasch,
665 T. B., Canagaratna, M. R., Jayne, J. T., and Worsnop, D. R.: A generalised method for the extraction of chemically
resolved mass spectra from aerodyne aerosol mass spectrometer data, *Journal of Aerosol Science*, 35, 909–922,
[10.1016/j.jaerosci.2004.02.007](https://doi.org/10.1016/j.jaerosci.2004.02.007), 2004.
- Allan, J. D., Williams, P. I., Morgan, W. T., Martin, C. L., Flynn, M. J., Lee, J., Nemitz, E., Phillips, G. J., Gallagher, M. W.,
and Coe, H.: Contributions from transport, solid fuel burning and cooking to primary organic aerosols in two UK
670 cities, *Atmos. Chem. Phys.*, 10, 647–668, <https://doi.org/10.5194/acp-10-647-2010>, 2010.
- Ban-Weiss, G. A., McLaughlin, J. P., Harley, R. A., Lunden, M. M., Kirchstetter, T. W., Kean, A. J., Strawa, A. W., Stevenson,
E. D., and Kendall, G. R.: Long-term changes in emissions of nitrogen oxides and particulate matter from on-road
gasoline and diesel vehicles, *Atmos. Environ.*, 42, 220–232, <https://doi.org/10.1016/j.atmosenv.2007.09.049>, 2008.
- Batmunkh, T., Kim, Y. J., Jung, J. S., Park, K., and Tumendemberel, B.: Chemical characteristics of fine particulate matters
675 measured during severe winter haze events in Ulaanbaatar, Mongolia, *J. Air Waste Manage.*, 63, 659–670,
<https://doi.org/10.1080/10962247.2013.776997>, 2013.



- 680 Canagaratna, M. R., Jayne, J. T., Jimenez, J. L., Allan, J. D., Alfarra, M. R., Zhang, Q., Onasch, T. B., Drewnick, F., Coe, H., Middlebrook, A., Delia, A., Williams, L. R., Trimborn, A. M., Northway, M. J., DeCarlo, P. F., Kolb, C. E., Davidovits, P., and Worsnop, D. R.: Chemical and microphysical characterization of ambient aerosols with the aerodyne aerosol mass spectrometer, *Mass Spectrom. Rev.*, 26, 185–222, <https://doi.org/10.1002/mas.20115>, 2007.
- Canagaratna, M. R., Jimenez, J. L., Kroll, J. H., Chen, Q., Kessler, S. H., Massoli, P., Ruiz, L. H., Fortner, E., Williams, L. R., Wilson, K. R., Surratt, J. D., Donahue, N. M., Jayne, J. T., and Worsnop, D. R.: Elemental ratio measurements of organic compounds using aerosol mass spectrometry: characterization, improved calibration, and implications, *Atmos. Chem. Phys.*, 15, 253–272, <https://doi.org/10.5194/acp-15-253-2015>, 2015.
- 685 Chen, G., Knibbs, L. D., Zhang, W., Li, S., Cao, W., Guo, J., Ren, H., Wang, B., Wang, H., Williams, G., Hamm, N. A. S., and Guo, Y.: Estimating spatiotemporal distribution of PM₁ concentrations in China with satellite remote sensing, meteorology, and land use information, *Environ. Pollut.*, 233, 1086–1094, <https://doi.org/10.1016/j.envpol.2017.10.011>, 2018.
- 690 Crippa, M., DeCarlo, P. F., Slowik, J. G., Mohr, C., Heringa, M. F., Chirico, R., Poulain, L., Freutel, F., Sciare, J., Cozic, J., Di Marco, C. F., Elsasser, M., Nicolas, J. B., Marchand, N., Abidi, E., Wiedensohler, A., Drewnick, F., Schneider, J., Borrmann, S., Nemitz, E., Zimmermann, R., Jaffrezo, J. L., Prévôt, A. S. H., and Baltensperger, U.: Wintertime aerosol chemical composition and source apportionment of the organic fraction in the metropolitan area of Paris, *Atmos. Chem. Phys.*, 13, 961–981, <https://doi.org/10.5194/acp-13-961-2013>, 2013.
- Dall'Osto, M., Ovadnevaite, J., Ceburnis, D., Martin, D., Healy, R. M., O'Connor, I. P., Kourtev, I., Sodeau, J. R., Wenger, J. C., and O'Dowd, C.: Characterization of urban aerosol in Cork city (Ireland) using aerosol mass spectrometry, *Atmos. Chem. Phys.*, 13, 4997–5015, <https://doi.org/10.5194/acp-13-4997-2013>, 2013.
- 695 De Laeter, J. R., Böhlke, J. K., De Bièvre, P., Hidaka, H., Peiser, H. S., Rosman, K. J. R., and Taylor, P. D. P.: Atomic weights of the elements. Review 2000 (IUPAC technical report), *Pure Appl. Chem.*, 75, 683–800, <https://doi.org/10.1351/pac200375060683>, 2003.
- 700 DeCarlo, P. F., Kimmel, J. R., Trimborn, A., Northway, M. J., Jayne, J. T., Aiken, A. C., Gonin, M., Fuhrer, K., Horvath, T., Docherty, K. S., Worsnop, D. R., and Jimenez, J. L.: Field-deployable, high-resolution, time-of-flight aerosol mass spectrometer, *Anal. Chem.*, 78, 8281–8289, <https://doi.org/10.1021/ac061249n>, 2006.
- Draxler, R. R., Stunder, B., Rolph, G., Stein, A., and Taylor, A.: HYSPLIT_4 User's Guide, available at http://www.arl.noaa.gov/documents/reports/hysplit_user_guide.pdf, NOAA Air Resources Laboratory, Silver Spring, Maryland, USA 2012.
- 705 Draxler, R. R. a. H., G. D.: Description of the HYSPLIT_4 modeling system, available at: <http://www.arl.noaa.gov/documents/reports/arl-224.pdf> (last access: 5 January 2014), NOAA Air Resources Laboratory, Silver Spring, Maryland, USA, 1997.



- 710 Ebenstein, A., Fan, M., Greenstone, M., He, G., and Zhou, M.: New evidence on the impact of sustained exposure to air pollution on life expectancy from China's Huai River Policy, *P. Natl. Acad. Sci. U. S. A.*, 114, 10384–10389, <https://doi.org/10.1073/pnas.1616784114>, 2017.
- 715 Elser, M., Huang, R.-J., Wolf, R., Slowik, J. G., Wang, Q., Canonaco, F., Li, G., Bozzetti, C., Daellenbach, K. R., Huang, Y., Zhang, R., Li, Z., Cao, J., Baltensperger, U., El-Haddad, I., and Prévôt, A. S. H.: New insights into PM_{2.5} chemical composition and sources in two major cities in China during extreme haze events using aerosol mass spectrometry, *Atmos. Chem. Phys.*, 16, 3207–3225, <https://doi.org/10.5194/acp-16-3207-2016>, 2016.
- Fontes, T., Li, P., Barros, N., and Zhao, P.: Trends of PM 2.5 concentrations in China: a long term approach, *J. Environ. Manage.*, 196, 719–732, <https://doi.org/10.1016/j.jenvman.2017.03.074>, 2017.
- 720 Ge, X., Setyan, A., Sun, Y., and Zhang, Q.: Primary and secondary organic aerosols in Fresno, California during wintertime: results from high resolution aerosol mass spectrometry, *J. Geophys. Res. Atmos.*, 117, D19301, <https://doi.org/10.1029/2012jd018026>, 2012a.
- Ge, X., Zhang, Q., Sun, Y., Ruehl, C. R., and Setyan, A.: Effect of aqueous-phase processing on aerosol chemistry and size distributions in Fresno, California, during wintertime, *Environ. Chem.*, 9, 221–235, <https://doi.org/10.1071/en11168>, 2012b.
- 725 Hayes, P. L., Ortega, A. M., Cubison, M. J., Froyd, K. D., Zhao, Y., Cliff, S. S., Hu, W. W., Toohey, D. W., Flynn, J. H., Lefter, B. L., Grossberg, N., Alvarez, S., Rappenglück, B., Taylor, J. W., Allan, J. D., Holloway, J. S., Gilman, J. B., Kuster, W. C., de Gouw, J. A., Massoli, P., Zhang, X., Liu, J., Weber, R. J., Corrigan, A. L., Russell, L. M., Isaacman, G., Worton, D. R., Kreisberg, N. M., Goldstein, A. H., Thalman, R., Waxman, E. M., Volkamer, R., Lin, Y. H., Surratt, J. D., Kleindienst, T. E., Offenberg, J. H., Dusanter, S., Griffith, S., Stevens, P. S., Brioude, J., Angevine, W. M., and Jimenez, J. L.: Organic aerosol composition and sources in Pasadena, California, during the 2010 CalNex campaign, *J. Geophys. Res. Atmos.*, 118, 9233–9257, <https://doi.org/10.1002/jgrd.50530>, 2013.
- 730 He, L.-Y., Hu, M., Huang, X.-F., Yu, B.-D., Zhang, Y.-H., and Liu, D.-Q.: Measurement of emissions of fine particulate organic matter from Chinese cooking, *Atmos. Environ.*, 38, 6557–6564, <https://doi.org/10.1016/j.atmosenv.2004.08.034>, 2004.
- 735 Heal, M. R., Hibbs, L. R., Agius, R. M., and Beverland, I. J.: Total and water-soluble trace metal content of urban background PM₁₀, PM_{2.5} and black smoke in Edinburgh, UK, *Atmos. Environ.*, 39, 1417–1430, <https://doi.org/10.1016/j.atmosenv.2004.11.026>, 2005.
- Heo, J. B., Hopke, P. K., and Yi, S. M.: Source apportionment of PM_{2.5} in Seoul, Korea, *Atmos. Chem. Phys.*, 9, 4957–4971, <https://doi.org/10.5194/acp-9-4957-2009>, 2009.
- 740 Herndon, S. C., Onasch, T. B., Wood, E. C., Kroll, J. H., Canagaratna, M. R., Jayne, J. T., Zavala, M. A., Knighton, W. B., Mazzoleni, C., Dubey, M. K., Ulbrich, I. M., Jimenez, J. L., Seila, R., de Gouw, J. A., de Foy, B., Fast, J., Molina, L. T., Kolb, C. E., and Worsnop, D. R.: Correlation of secondary organic aerosol with odd oxygen in Mexico City, *Geophys. Res. Lett.*, 35, L15804, <https://doi.org/10.1029/2008gl034058>, 2008.



- Hu, W. W., Hu, M., Yuan, B., Jimenez, J. L., Tang, Q., Peng, J. F., Hu, W., Shao, M., Wang, M., Zeng, L. M., Wu, Y. S., Gong, Z. H., Huang, X. F., and He, L. Y.: Insights on organic aerosol aging and the influence of coal combustion at a regional receptor site of central eastern China, *Atmos. Chem. Phys.*, 13, 10095–10112, <https://doi.org/10.5194/acp-13-10095-2013>, 2013.
- 745
- Huang, X. F., He, L. Y., Hu, M., Canagaratna, M. R., Sun, Y., Zhang, Q., Zhu, T., Xue, L., Zeng, L. W., Liu, X. G., Zhang, Y. H., Jayne, J. T., Ng, N. L., and Worsnop, D. R.: Highly time-resolved chemical characterization of atmospheric submicron particles during 2008 Beijing Olympic Games using an aerodyne high-resolution aerosol mass spectrometer, *Atmos. Chem. Phys.*, 10, 8933–8945, <https://doi.org/10.5194/acp-10-8933-2010>, 2010.
- 750
- IPCC: Summary for policymakers, in: *Climate Change 2013: The Physical Science Basis*, edited by: Stocker, T. F., Qin, D., Plattner, G.-K., Tignor, M., Allen, S. K., Boschung, J., Nauels, A., Xia, Y., Bex, V., and Midgley, P. M., Cambridge University Press, Cambridge, UK, New York, NY, USA, 3–29, 2013.
- Jayne, J. T., Leard, D. C., Zhang, X., Davidovits, P., Smith, K. A., Kolb, C. E., and Worsnop, D. R.: Development of an aerosol mass spectrometer for size and composition analysis of submicron particles, *Aerosol Sci. Technol.*, 33, 49–70, <https://doi.org/10.1080/027868200410840>, 2000.
- 755
- Jung, J., Tsatsral, B., Kim, Y. J., and Kawamura, K.: Organic and inorganic aerosol compositions in Ulaanbaatar, Mongolia, during the cold winter of 2007 to 2008: dicarboxylic acids, ketocarboxylic acids, and α -dicarbonyls, *J. Geophys. Res.*, 115, <https://doi.org/10.1029/2010jd014339>, 2010.
- 760
- Jung, J., Lyu, Y., Lee, M., Hwang, T., Lee, S., and Oh, S.: Impact of Siberian forest fires on the atmosphere over the Korean Peninsula during summer 2014, *Atmospheric Chemistry and Physics*, 16, 6757–6770, [10.5194/acp-16-6757-2016](https://doi.org/10.5194/acp-16-6757-2016), 2016.
- Kim, E., Hopke, P. K., and Edgerton, E. S.: Source identification of Atlanta aerosol by positive matrix factorization, *Journal of the Air & Waste Management Association*, 53, 731–739, 2003.
- 765
- Kim, H., and Zhang, Q.: Chemistry of new particle growth during springtime in the Seoul metropolitan area, Korea, *Chemosphere*, 225, 713–722, <https://doi.org/10.1016/j.chemosphere.2019.03.072>, 2019.
- Kim, H., Zhang, Q., and Heo, J.: Influence of intense secondary aerosol formation and long-range transport on aerosol chemistry and properties in the Seoul Metropolitan Area during spring time: results from KORUS-AQ, *Atmos. Chem. Phys.*, 18, 7149–7168, <https://doi.org/10.5194/acp-18-7149-2018>, 2018.
- 770
- Kim, H., Zhang, Q., Bae, G.-N., Kim, J. Y., and Lee, S. B.: Sources and atmospheric processing of winter aerosols in Seoul, Korea: insights from real-time measurements using a high-resolution aerosol mass spectrometer, *Atmos. Chem. Phys.*, 17, 2009–2033, <https://doi.org/10.5194/acp-17-2009-2017>, 2017.
- Kummer, U., Pacyna, J., Pacyna, E., and Friedrich, R.: Assessment of heavy metal releases from the use phase of road transport in Europe, *Atmos. Environ.*, 43, 640–647, <https://doi.org/10.1016/j.atmosenv.2008.10.007>, 2009.
- 775
- Kuwata, M., Zorn, S. R., and Martin, S. T.: Using elemental ratios to predict the density of organic material composed of carbon, hydrogen, and oxygen, *Environ. Sci. Technol.*, 46, 787–794, <https://doi.org/10.1021/es202525q>, 2012.



- Lough, G. C., Schauer, J. J., Park, J.-S., Shafer, M. M., DeMinter, J. T., and Weinstein, J. P.: Emissions of metals associated with motor vehicle roadways, *Environ. Sci. Technol.*, 39, 826–836, <https://doi.org/10.1021/es048715f>, 2005.
- 780 Middlebrook, A. M., Bahreini, R., Jimenez, J. L., and Canagaratna, M. R.: Evaluation of composition-dependent collection efficiencies for the aerodyne aerosol mass spectrometer using field data, *Aerosol Sci. Technol.*, 46, 258–271, <https://doi.org/10.1080/02786826.2011.620041>, 2012.
- MOE, Ministry of Environment, Korea (2016). *White Paper of Environment*, Seoul.
- Mohr, C., DeCarlo, P. F., Heringa, M. F., Chirico, R., Slowik, J. G., Richter, R., Reche, C., Alastuey, A., Querol, X., Seco, R., Peñuelas, J., Jiménez, J. L., Crippa, M., Zimmermann, R., Baltensperger, U., and Prévôt, A. S. H.: Identification and
785 quantification of organic aerosol from cooking and other sources in Barcelona using aerosol mass spectrometer data, *Atmos. Chem. Phys.*, 12, 1649–1665, <https://doi.org/10.5194/acp-12-1649-2012>, 2012.
- Mohr, C., Huffman, J. A., Cubison, M. J., Aiken, A. C., Docherty, K. S., Kimmel, J. R., Ulbrich, I. M., Hannigan, M., and Jimenez, J. L.: Characterization of primary organic aerosol emissions from meat cooking, trash burning, and motor
790 vehicles with high-resolution aerosol mass spectrometry and comparison with ambient and chamber observations, *Environ. Sci. Technol.*, 43, 2443–2449, <https://doi.org/10.1021/es8011518>, 2009.
- Murphy, D. M., Hudson, P. K., Cziczo, D. J., Gallavardin, S., Froyd, K. D., Johnston, M. V., Middlebrook, A. M., Reinard, M. S., Thomson, D. S., Thornberry, T., and Wexler, A. S.: Distribution of lead in single atmospheric particles, *Atmos. Chem. Phys.*, 7, 3195–3210, <https://doi.org/10.5194/acp-7-3195-2007>, 2007.
- Nault, B. A., Campuzano-Jost, P., Day, D. A., Schroder, J. C., Anderson, B., Beyersdorf, A. J., Blake, D. R., Brune, W. H.,
795 Choi, Y., Corr, C. A., de Gouw, J. A., Dibb, J., DiGangi, J. P., Diskin, G. S., Fried, A., Huey, L. G., Kim, M. J., Knote, C. J., Lamb, K. D., Lee, T., Park, T., Pusede, S. E., Scheuer, E., Thornhill, K. L., Woo, J.-H., and Jimenez, J. L.: Secondary organic aerosol production from local emissions dominates the organic aerosol budget over Seoul, South Korea, during KORUS-AQ, *Atmos. Chem. Phys.*, 18, 17769–17800, <https://doi.org/10.5194/acp-18-17769-2018>, 2018.
- 800 Oh, H.-R., Ho, C.-H., Koo, Y.-S., Baek, K.-G., Yun, H.-Y., Hur, S.-K., Choi, D.-R., Jhun, J.-G., and Shim, J.-S.: Impact of Chinese air pollutants on a record-breaking PMs episode in the Republic of Korea for 11–15 January 2019, *Atmos. Environ.*, 223, 117262, <https://doi.org/10.1016/j.atmosenv.2020.117262>, 2020.
- Paatero, P., and Tapper, U.: Positive matrix factorization: A non-negative factor model with optimal utilization of error estimates of data values, *Environmetrics*, 5, 111–126, 10.1002/env.3170050203, 1994.
- 805 Peterson, D. A., Hyer, E. J., Han, S.-O., Crawford, J. H., Park, R. J., Holz, R., Kuehn, R. E., Eloranta, E., Knote, C., Jordan, C. E., and Lefer, B. L.: Meteorology influencing springtime air quality, pollution transport, and visibility in Korea, *Elementa: Science of the Anthropocene*, 7, 57, <https://doi.org/10.1525/elementa.395>, 2019.
- Pope III, C. A., and Dockery, D. W.: Health Effects of Fine Particulate Air Pollution: Lines that Connect, *Journal of the Air & Waste Management Association*, 56, 709–742, 2006.



- 810 Pöschl, U.: Atmospheric Aerosols: Composition, Transformation, Climate and Health Effects, *Angewandte Chemie International Edition*, 44, 7520–7540, 10.1002/anie.200501122, 2005.
- Quan, J., Tie, X., Zhang, Q., Liu, Q., Li, X., Gao, Y., and Zhao, D.: Characteristics of heavy aerosol pollution during the 2012–2013 winter in Beijing, China, *Atmos. Environ.*, 88, 83–89, <https://doi.org/10.1016/j.atmosenv.2014.01.058>, 2014.
- 815 Reff, A., Bhave, P. V., Simon, H., Pace, T. G., Pouliot, G. A., Mobley, J. D., and Houyoux, M.: Emissions inventory of PM_{2.5} trace elements across the United States, *Environ. Sci. Technol.*, 43, 5790–5796, <https://doi.org/10.1021/es802930x>, 2009.
- Salcedo, D., Onasch, T. B., Aiken, A. C., Williams, L. R., de Foy, B., Cubison, M. J., Worsnop, D. R., Molina, L. T., and Jimenez, J. L.: Determination of particulate lead using aerosol mass spectrometry: MILAGRO/MCMA-2006 observations, *Atmos. Chem. Phys.*, 10, 5371–5389, <https://doi.org/10.5194/acp-10-5371-2010>, 2010.
- 820 Schroeder, J. R., Crawford, J. H., Ahn, J.-Y., Chang, L., Fried, A., Walega, J., Weinheimer, A., Montzka, D. D., Hall, S. R., Ullmann, K., Wisthaler, A., Mikoviny, T., Chen, G., Blake, D. R., Blake, N. J., Hughes, S. C., Meinardi, S., Diskin, G., Digangi, J. P., Choi, Y., Pusede, S. E., Huey, G. L., Tanner, D. J., Kim, M., and Wennberg, P.: Observation-based modeling of ozone chemistry in the Seoul metropolitan area during the Korea-United States Air Quality Study (KORUS-AQ), *Elementa: Science of the Anthropocene*, 8, 3, <https://doi.org/10.1525/elementa.400>, 2020.
- 825 Simoneit, B. R. T., Rushdi, A. I., bin Abas, M. R., and Didyk, B. M.: Alkyl Amides and Nitriles as Novel Tracers for Biomass Burning, *Environmental Science & Technology*, 37, 16–21, 10.1021/es020811y, 2003.
- Sun, Y., Du, W., Fu, P., Wang, Q., Li, J., Ge, X., Zhang, Q., Zhu, C., Ren, L., Xu, W., Zhao, J., Han, T., Worsnop, D. R., and Wang, Z.: Primary and secondary aerosols in Beijing in winter: sources, variations and processes, *Atmos. Chem. Phys.*, 16, 8309–8329, <https://doi.org/10.5194/acp-16-8309-2016>, 2016a.
- 830 Sun, Y., Du, W., Fu, P., Wang, Q., Li, J., Ge, X., Zhang, Q., Zhu, C., Ren, L., Xu, W., Zhao, J., Han, T., Worsnop, D. R., and Wang, Z.: Primary and secondary aerosols in Beijing in winter: sources, variations and processes, *Atmos. Chem. Phys.*, 16, 8309–8329, <https://doi.org/10.5194/acp-16-8309-2016>, 2016b.
- Sun, Y., Jiang, Q., Wang, Z., Fu, P., Li, J., Yang, T., and Yin, Y.: Investigation of the sources and evolution processes of severe haze pollution in Beijing in January 2013, *J. Geophys. Res. Atmos.*, 119, 4380–4398, <https://doi.org/10.1002/2014jd021641>, 2014.
- 835 Sun, Y., Wang, Z., Fu, P., Jiang, Q., Yang, T., Li, J., and Ge, X.: The impact of relative humidity on aerosol composition and evolution processes during wintertime in Beijing, China, *Atmos. Environ.*, 77, 927–934, <https://doi.org/10.1016/j.atmosenv.2013.06.019>, 2013.
- Sun, Y., Zhang, Q., Zheng, M., Ding, X., Edgerton, E. S., and Wang, X.: Characterization and source apportionment of water-soluble organic matter in atmospheric fine particles (PM_{2.5}) with high-resolution aerosol mass spectrometry and GC–MS, *Environ. Sci. Technol.*, 45, 4854–4861, <https://doi.org/10.1021/es200162h>, 2011.
- 840



- Ulbrich, I. M., Canagaratna, M. R., Zhang, Q., Worsnop, D. R., and Jimenez, J. L.: Interpretation of organic components from Positive Matrix Factorization of aerosol mass spectrometric data, *Atmospheric Chemistry and Physics*, 9, 2891–2918, 10.5194/acp-9-2891-2009, 2009.
- 845 Wang, X., Williams, B. J., Wang, X., Tang, Y., Huang, Y., Kong, L., Yang, X., and Biswas, P.: Characterization of organic aerosol produced during pulverized coal combustion in a drop tube furnace, *Atmos. Chem. Phys.*, 13, 10919–10932, <https://doi.org/10.5194/acp-13-10919-2013>, 2013.
- Watson, J. G.: Visibility: science and regulation, *JAPCA J. Air Waste MA*, 52, 628–713, <https://doi.org/10.1080/10473289.2002.10470813>, 2002.
- 850 Xu, J., Shi, J., Zhang, Q., Ge, X., Canonaco, F., Prévôt, A. S. H., Vonwiller, M., Szidat, S., Ge, J., Ma, J., An, Y., Kang, S., and Qin, D.: Wintertime organic and inorganic aerosols in Lanzhou, China: sources, processes and comparison with the results during summer, *Atmos. Chem. Phys.*, 16, 14937–14957, <https://doi.org/10.5194/acp-16-14937-2016>, 2016.
- Xu, L., Guo, H., Boyd, C. M., Klein, M., Bougiatioti, A., Cerully, K. M., Hite, J. R., Isaacman-VanWertz, G., Kreisberg, N. M., Knote, C., Olson, K., Koss, A., Goldstein, A. H., Hering, S. V., de Gouw, J., Baumann, K., Lee, S.-H., Nenes, A., Weber, R. J., and Ng, N. L.: Effects of anthropogenic emissions on aerosol formation from isoprene and monoterpenes in the southeastern United States, *P. Natl. Acad. Sci. U. S. A.*, 112, 37–42, <https://doi.org/10.1073/pnas.1417609112>, 2015.
- 855 Xu, W., Sun, Y., Wang, Q., Zhao, J., Wang, J., Ge, X., Xie, C., Zhou, W., Du, W., Li, J., Fu, P., Wang, Z., Worsnop, D. R., and Coe, H.: Changes in aerosol chemistry from 2014 to 2016 in winter in Beijing: insights from high-resolution aerosol mass spectrometry, *J. Geophys. Res. Atmos.*, 124, 1132–1147, <https://doi.org/10.1029/2018jd029245>, 2019.
- Young, D. E., Kim, H., Parworth, C., Zhou, S., Zhang, X., Cappa, C. D., Seco, R., Kim, S., and Zhang, Q.: Influences of emission sources and meteorology on aerosol chemistry in a polluted urban environment: results from DISCOVER-AQ California, *Atmos. Chem. Phys.*, 16, 5427–5451, <https://doi.org/10.5194/acp-16-5427-2016>, 2016.
- 865 Zhang, Q. H., Zhang, J. P., and Xue, H. W.: The challenge of improving visibility in Beijing, *Atmos. Chem. Phys.*, 10, 7821–7827, <https://doi.org/10.5194/acp-10-7821-2010>, 2010.
- Zhang, Q., Alfarra, M. R., Worsnop, D. R., Allan, J. D., Coe, H., Canagaratna, M. R., and Jimenez, J. L.: Deconvolution and quantification of hydrocarbon-like and oxygenated organic aerosols based on aerosol mass spectrometry, *Environ. Sci. Technol.*, 39, 4938–4952, <https://doi.org/10.1021/es048568l>, 2005a.
- 870 Zhang, Q., Jimenez, J. L., Canagaratna, M. R., Ulbrich, I. M., Ng, N. L., Worsnop, D. R., and Sun, Y.: Understanding atmospheric organic aerosols via factor analysis of aerosol mass spectrometry: a review, *Anal. Bioanal. Chem.*, 401, 3045–3067, <https://doi.org/10.1007/s00216-011-5355-y>, 2011.
- Zhang, Q., Worsnop, D. R., Canagaratna, M. R., and Jimenez, J. L.: Hydrocarbon-like and oxygenated organic aerosols in Pittsburgh: insights into sources and processes of organic aerosols, *Atmos. Chem. Phys.*, 5, 3289–3311, 875 <https://doi.org/10.5194/acp-5-3289-2005>, 2005b.



- Zhang, Y. J., Tang, L. L., Wang, Z., Yu, H. X., Sun, Y. L., Liu, D., Qin, W., Canonaco, F., Prévôt, A. S. H., Zhang, H. L., and Zhou, H. C.: Insights into characteristics, sources, and evolution of submicron aerosols during harvest seasons in the Yangtze River delta region, China, *Atmos. Chem. Phys.*, 15, 1331–1349, <https://doi.org/10.5194/acp-15-1331-2015>, 2015.
- 880 Zhao, J., Du, W., Zhang, Y., Wang, Q., Chen, C., Xu, W., Han, T., Wang, Y., Fu, P., Wang, Z., Li, Z., and Sun, Y.: Insights into aerosol chemistry during the 2015 China Victory Day parade: results from simultaneous measurements at ground level and 260 m in Beijing, *Atmos. Chem. Phys.*, 17, 3215–3232, <https://doi.org/10.5194/acp-17-3215-2017>, 2017.
- Zhao, P., Dong, F., Yang, Y., He, D., Zhao, X., Zhang, W., Yao, Q., and Liu, H.: Characteristics of carbonaceous aerosol in the region of Beijing, Tianjin, and Hebei, China, *Atmos. Environ.*, 71, 389–398, <https://doi.org/10.1016/j.atmosenv.2013.02.010>, 2013.
- 885 Zheng, G. J., Duan, F. K., Su, H., Ma, Y. L., Cheng, Y., Zheng, B., Zhang, Q., Huang, T., Kimoto, T., Chang, D., Pöschl, U., Cheng, Y. F., and He, K. B.: Exploring the severe winter haze in Beijing: the impact of synoptic weather, regional transport and heterogeneous reactions, *Atmos. Chem. Phys.*, 15, 2969–2983, <https://doi.org/10.5194/acp-15-2969-2015>, 2015.

890

895

900



905 Tables

Table 1: Correlation coefficient (Pearson's r) for the linear regression between the factors of the organic aerosols (OA) and the various particle- and gas-phase species and ions.

| Sources | r | HOA | COA | SFOA | LO-OOA1 | LO-OOA2 | MO-OOA1 | MO-OOA2 |
|---------------------|--|-------------|-------------|-------------|---------|-------------|-------------|-------------|
| Secondary inorganic | Nitrate | 0.29 | 0.17 | 0.22 | 0.52 | 0.89 | 0.33 | 0.89 |
| | Sulfate | 0.04 | -0.04 | 0.02 | 0.62 | 0.75 | 0.39 | 0.91 |
| | Ammonium | 0.24 | 0.11 | 0.18 | 0.57 | 0.87 | 0.36 | 0.93 |
| Gas | O ₃ | -0.56 | -0.45 | -0.41 | 0.16 | -0.07 | 0.05 | 0.09 |
| | NO ₂ | 0.62 | 0.62 | 0.56 | 0.04 | 0.30 | 0.00 | 0.25 |
| | CO | 0.62 | 0.41 | 0.61 | 0.12 | 0.41 | 0.24 | 0.54 |
| | SO ₂ | 0.29 | 0.26 | 0.29 | 0.14 | 0.30 | -0.04 | 0.29 |
| Secondary organic | CH ₂ SO ₂ ⁺ (79) | 0.26 | 0.14 | 0.21 | 0.41 | 0.84 | 0.30 | 0.75 |
| | CH ₃ SO ₂ ⁺ (79) | 0.28 | 0.17 | 0.21 | 0.39 | 0.87 | 0.30 | 0.73 |
| | CH ₄ SO ₃ ⁺ (96) | 0.25 | 0.14 | 0.19 | 0.40 | 0.82 | 0.26 | 0.72 |
| | C ₂ H ₃ O ⁺ (43) | 0.44 | 0.38 | 0.60 | 0.24 | 0.80 | 0.63 | 0.80 |
| | CO ₂ ⁺ (44) | 0.29 | 0.21 | 0.44 | 0.42 | 0.76 | 0.67 | 0.91 |
| Vehicle and primary | C ₃ H ₇ ⁺ (43) | 0.86 | 0.86 | 0.72 | -0.06 | 0.28 | 0.20 | 0.27 |
| | C ₄ H ₇ ⁺ (55) | 0.80 | 0.89 | 0.70 | -0.02 | 0.34 | 0.21 | 0.31 |
| | C ₄ H ₉ ⁺ (57) | 0.92 | 0.81 | 0.69 | -0.06 | 0.24 | 0.16 | 0.24 |
| | C ₅ H ₁₁ ⁺ (71) | 0.94 | 0.77 | 0.68 | -0.06 | 0.22 | 0.15 | 0.22 |
| Cooking | C ₃ H ₃ O ⁺ (55) | 0.56 | 0.78 | 0.70 | 0.08 | 0.56 | 0.51 | 0.57 |
| | C ₅ H ₈ O ⁺ (84) | 0.58 | 0.94 | 0.62 | -0.01 | 0.35 | 0.22 | 0.31 |
| | C ₆ H ₁₀ O ⁺ (98) | 0.54 | 0.98 | 0.56 | -0.09 | 0.18 | 0.12 | 0.14 |
| | C ₇ H ₁₂ O ⁺ (112) | 0.52 | 0.85 | 0.56 | -0.03 | 0.32 | 0.18 | 0.27 |
| Burning | C ₂ H ₄ O ₂ ⁺ (60) | 0.66 | 0.61 | 0.89 | -0.16 | 0.29 | 0.69 | 0.44 |
| | C ₃ H ₅ O ₂ ⁺ (73) | 0.65 | 0.71 | 0.85 | -0.10 | 0.36 | 0.65 | 0.49 |
| | Chloride | 0.61 | 0.19 | 0.45 | 0.19 | 0.52 | 0.34 | 0.56 |
| | BC | 0.59 | 0.43 | 0.66 | 0.21 | 0.48 | 0.30 | 0.68 |
| | PAH | 0.56 | 0.65 | 0.75 | -0.26 | -0.06 | 0.18 | 0.04 |
| | K (AMS) | 0.43 | 0.40 | 0.55 | 0.14 | 0.34 | 0.45 | 0.52 |
| CHN | CN ⁺ (26) | 0.31 | 0.21 | 0.39 | 0.44 | 0.68 | 0.51 | 0.89 |
| | CHN ⁺ (27) | 0.33 | 0.22 | 0.41 | 0.47 | 0.72 | 0.54 | 0.94 |
| | C ₃ H ₅ N ⁺ (55) | 0.55 | 0.49 | 0.59 | 0.21 | 0.72 | 0.47 | 0.75 |
| | C ₃ H ₇ N ⁺ (57) | 0.67 | 0.63 | 0.70 | -0.07 | 0.41 | 0.36 | 0.43 |
| Coal combustion | C ₉ H ₇ ⁺ (115) | 0.71 | 0.77 | 0.81 | 0.01 | 0.47 | 0.42 | 0.49 |
| | Pb | 0.47 | 0.31 | 0.60 | 0.24 | 0.73 | 0.49 | 0.62 |

BC, black carbon; PAH, polycyclic aromatic hydrocarbons.

The values with $r > 0.7$ are boldfaced.



Table 2: Comparison of the aerosol properties and meteorological parameters between the high- and low-loading periods.

| | | Overall I Period | EP1 | EP2 | EP3 | Haze | Clean | Ratio ^a (H/L) | Ratio ^b (E/L) |
|--|------------------------------------|------------------------|--------|--------|--------|--------|--------|-----------------------------|-----------------------------|
| PM1 species and ions ($\mu\text{g m}^{-3}$) | PM1+BC | 35.07 | 59.75 | 54.34 | 57.52 | 57.20 | 15.36 | 3.72 | 2.28 |
| | NO3 | 10.61 | 19.62 | 17.94 | 21.52 | 19.69 | 3.00 | 6.56 | 3.53 |
| | SO4 | 4.20 | 7.53 | 7.50 | 5.34 | 6.79 | 2.35 | 2.88 | 1.78 |
| | NH4 | 4.70 | 8.68 | 8.03 | 8.22 | 8.31 | 1.72 | 4.83 | 2.73 |
| | BC | 1.60 | 2.95 | 2.03 | 1.94 | 2.31 | 0.71 | 3.23 | 2.24 |
| | Chl | 0.60 | 0.90 | 1.13 | 0.73 | 0.92 | 0.23 | 3.93 | 2.57 |
| | Org | 13.35 | 20.04 | 17.72 | 19.74 | 19.17 | 7.34 | 2.61 | 1.82 |
| | PAH | 9.11 | 13.87 | 10.97 | 11.41 | 12.08 | 5.25 | 4.66 | 1.73 |
| | Pb | 0.0027 | 0.0045 | 0.0035 | 0.0035 | 0.0039 | 0.0014 | 2.65 | 1.89 |
| | C9H7 | 0.016 | 0.0226 | 0.020 | 0.025 | 0.022 | 0.008 | 2.807 | 1.997 |
| Sources of the OA ($\mu\text{g m}^{-3}$) | HOA | 0.98 | 1.33 | 0.82 | 1.74 | 1.30 | 0.25 | 5.15 | 3.92 |
| | COA | 1.74 | 2.26 | 1.27 | 3.16 | 2.23 | 0.48 | 4.66 | 3.64 |
| | BBOA | 2.11 | 3.15 | 2.12 | 2.79 | 2.68 | 1.16 | 2.32 | 1.82 |
| | LOOOA1 | 2.08 | 2.88 | 1.79 | 2.67 | 2.45 | 1.54 | 1.58 | 1.35 |
| | LOOOA2 | 1.88 | 2.85 | 3.81 | 5.77 | 4.15 | 0.39 | 10.71 | 4.87 |
| | MOOOA1 | 2.32 | 2.88 | 3.91 | 3.32 | 3.37 | 2.56 | 1.31 | 0.91 |
| | MOOOA2 | 1.82 | 4.35 | 3.60 | 3.58 | 3.85 | 0.71 | 5.42 | 2.56 |
| Gases (ppb) | NO2 | 37.24 | 49.67 | 41.24 | 52.88 | 47.93 | 20.27 | 2.36 | 1.84 |
| | CO | 0.89 | 1.26 | 1.12 | 1.15 | 1.18 | 0.57 | 2.06 | 1.55 |
| | SO2 | 3.93 | 4.72 | 3.68 | 4.41 | 4.27 | 3.07 | 1.39 | 1.28 |
| | O3 | 23.04 | 28.16 | 21.49 | 13.84 | 21.16 | 31.81 | 0.67 | 0.72 |
| Meteorolo gical parameters | RH (%) | 48.15 | 46.36 | 66.32 | 64.67 | 59.12 | 46.34 | 1.28 | 1.04 |
| | WS (m/s) | 2.01 | 1.79 | 1.92 | 1.39 | 1.70 | 2.71 | 0.63 | 0.74 |
| | Temperature ($^{\circ}\text{C}$) | 4.70 | 8.42 | 5.98 | 9.98 | 8.13 | 4.71 | 1.73 | 1.00 |
| Ratios | NOR | 0.09 | 0.13 | 0.15 | 0.17 | 0.15 | 0.06 | 2.71 | 1.66 |
| | SOR | 0.19 | 0.26 | 0.32 | 0.27 | 0.28 | 0.15 | 1.90 | 1.27 |
| | O/C | 0.52 | 0.55 | 0.57 | 0.47 | 0.53 | 0.59 | 0.90 | 0.89 |
| | H/C | 1.61 | 1.58 | 1.59 | 1.65 | 1.60 | 1.57 | 1.02 | 1.03 |
| | OM/OC | 1.86 | 1.90 | 1.92 | 1.80 | 1.87 | 1.94 | 0.96 | 0.96 |

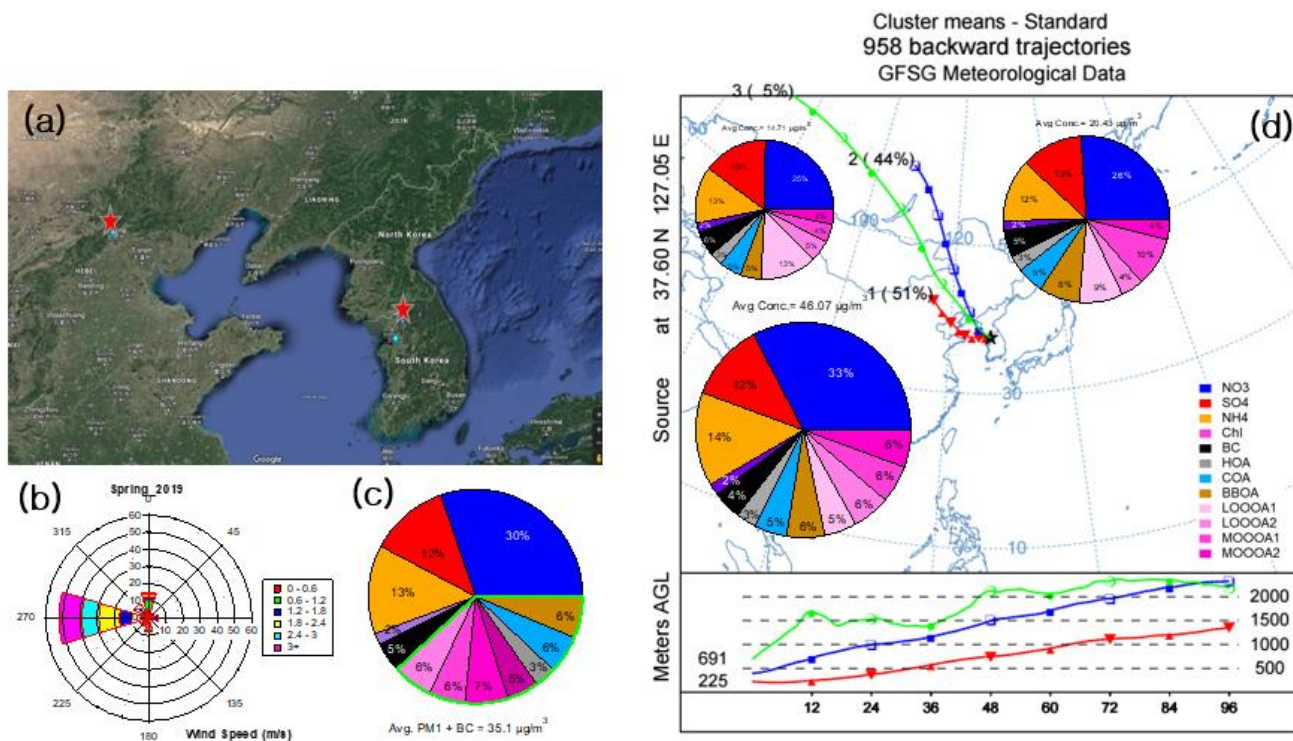
^a Ratios of haze/clean days

^b Ratios of overall/clean period



915

Figures



920

925 **Figure 1:** (a) © Google map image of the measurement sites in the SMA in Korea and Beijing in China; (b) wind rose plot for the entire study period; (c) average compositional pie chart of the PM₁ species and each of the factors of the OA during the whole campaign. The green outline indicates the fraction of the total OA; (d) averaged compositional pie chart of the PM₁ species (nonrefractory-PM₁ plus black carbon (BC)) in the three different clusters. The trajectories were released at half of the mixing height at the KIST site (latitude: 37.60°N; longitude: 127.05°E) during the entire period.



930

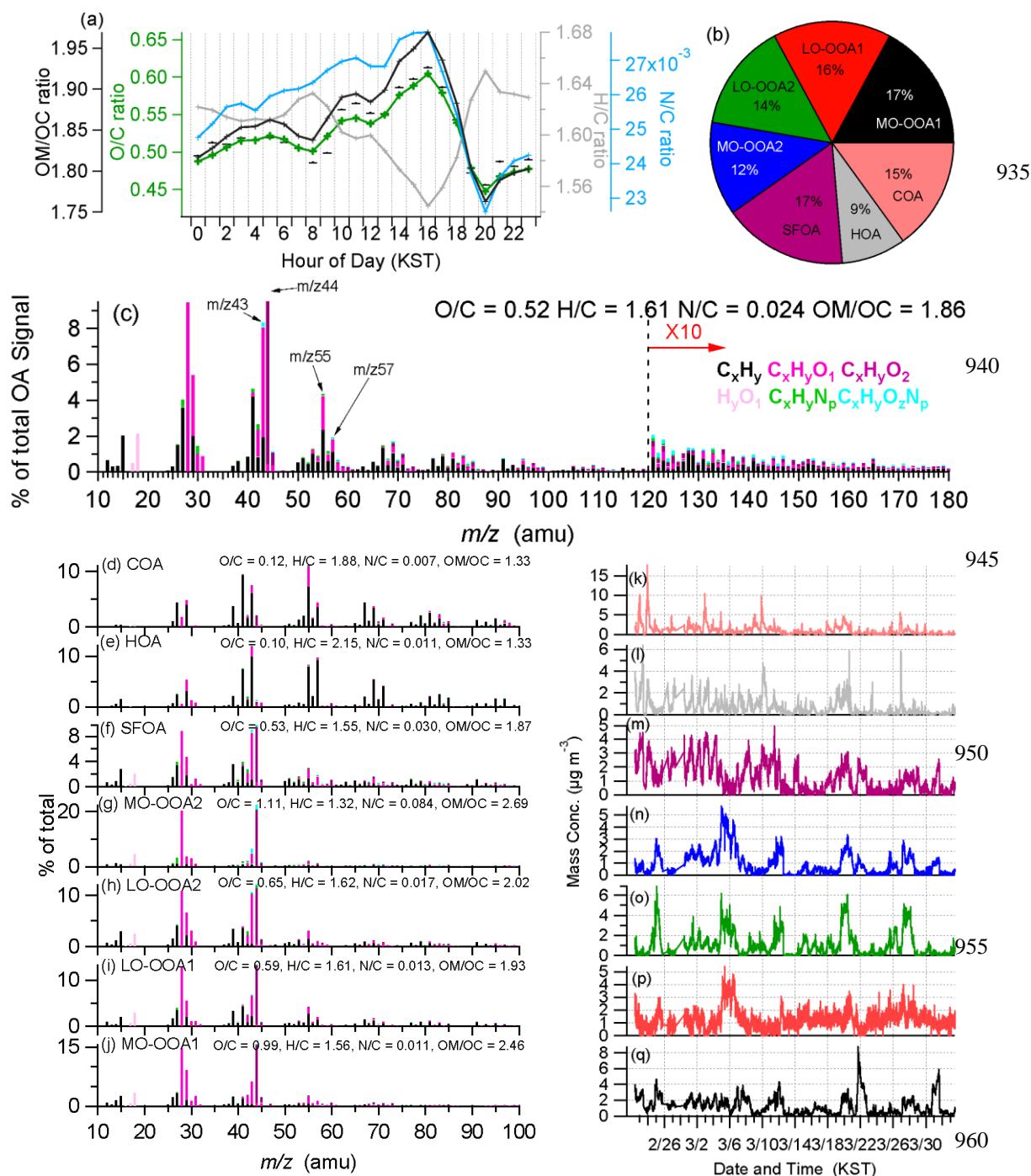
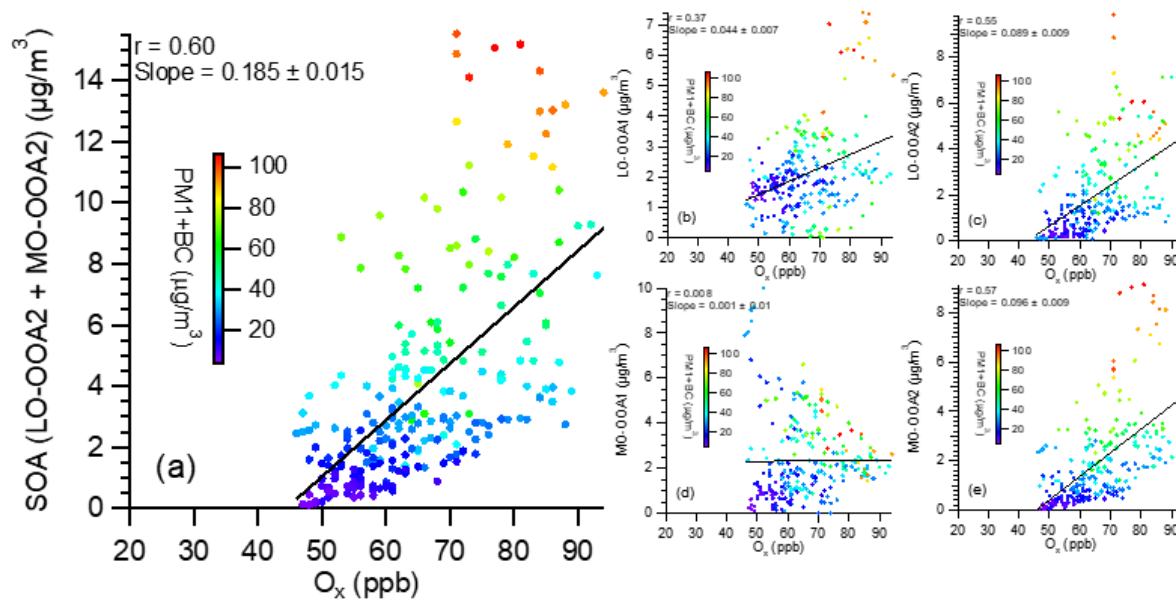


Figure 2: (a) Average diurnal profiles of the organic matter to the organic carbon (OM/OC) ratio, oxygen to carbon (O/C), hydrogen to carbon (H/C) ratio, and nitrogen-to-carbon (N/C) ratio, where the O/C, H/C and OM/OC elemental ratios were determined using the updated method (Canagaratna et al., 2015); (b) compositional pie chart of the average fractional contribution of each of the



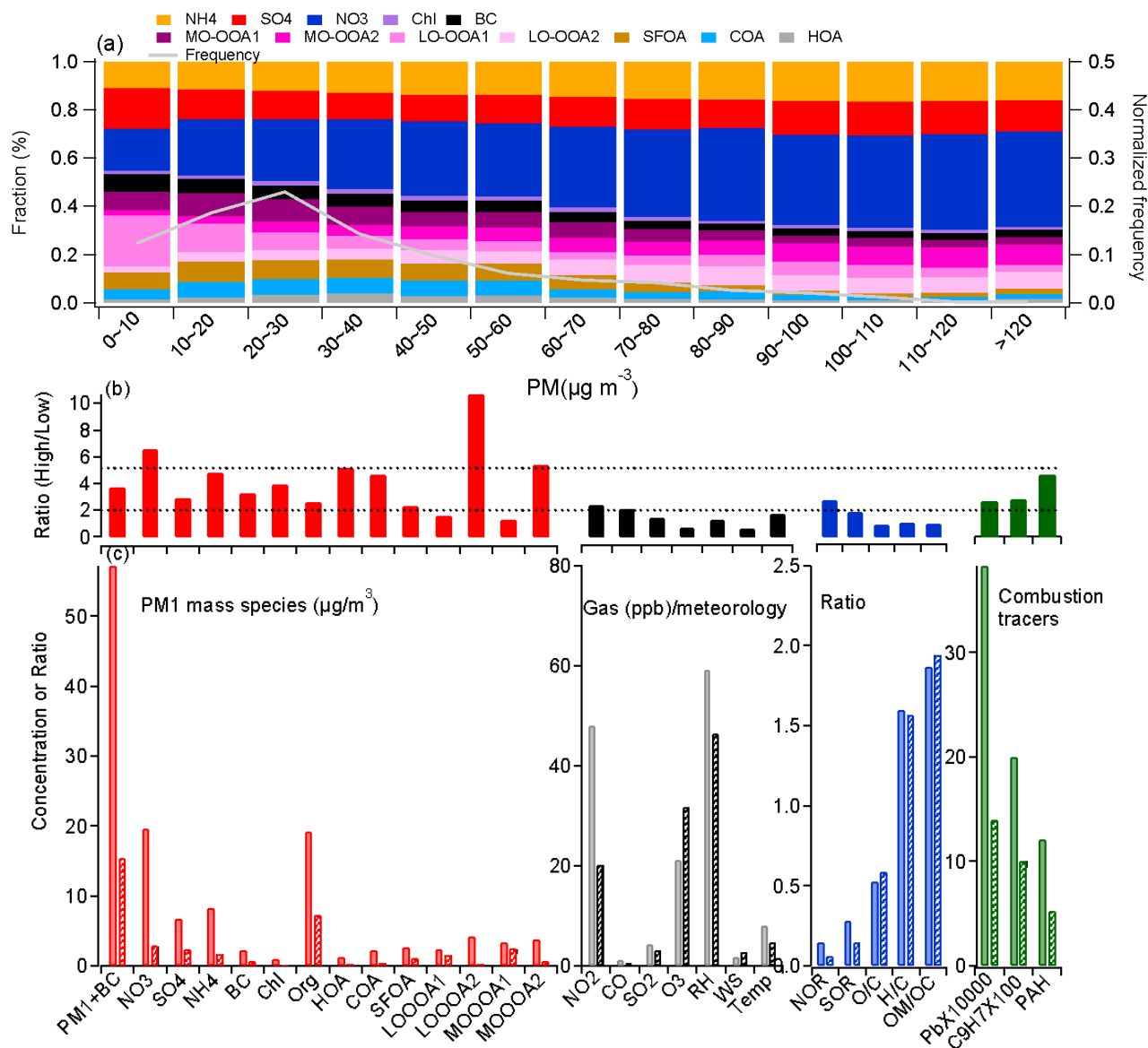
965 factors of the OA to the total OA during the campaign; (c) average high-resolution mass spectra of the OA colored by the different
ion families. The average elemental ratios for the fractions of the OA are described; (d-j) high-resolution mass spectra of all organic
sources from the PMF analysis including cooking OA (COA), hydrocarbon-like OA (HOA), solid fuel burning OA (SFOA), more
oxidized OA2 (MO-OOA2), less oxidized OA2 (LO-OOA2), less oxidized OA1 (LO-OOA1), and more oxidized OA1 (MO-OOA1).
(c) Semivolatile oxygenated OA (SV-OOA), and (k-q) time series of each organic source from the PMA analysis including COA,
970 HOA, SFOA, MO-OOA2, LO-OOA2, LO-OOA1 and MO-OOA1 (from top to bottom).



975

Figure 3: Scatter plots of (a) SOA; (b) LO-OOA1; (c) LO-OOA2; (d) MO-OOA1; (e) MO-OOA2 vs O_x during the daytime (10:00 - 16:00) in the early spring of 2019. Note that the fitting for the SOAs includes only the LO-OOA2 and MO-OOA2, which exhibited a good correlation with O_x .

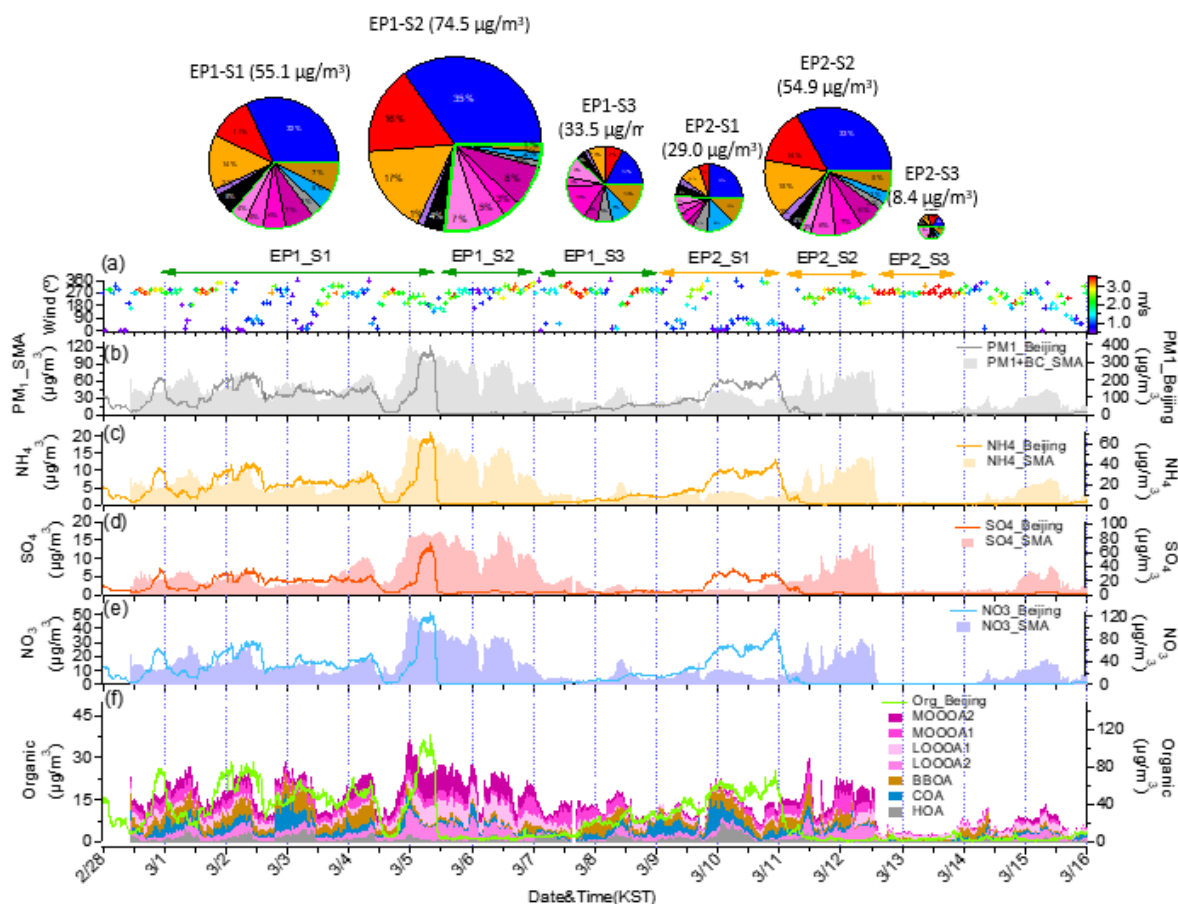
980



985

990

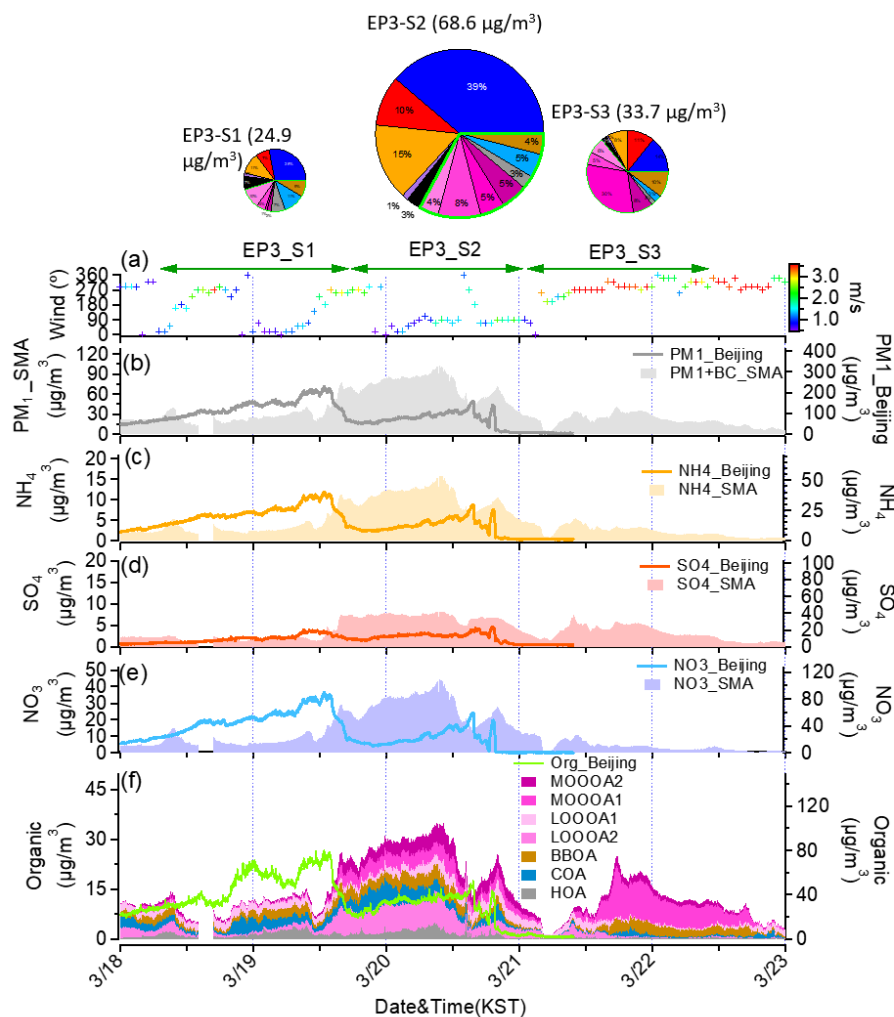
Figure 4: (a) Variation in the PM₁+BC composition as a function of the PM₁+BC mass concentration during the entire period. The probabilities of the PM₁ mass during the study period are also shown on the right axis; (b) the ratios of the absolute concentration of PM₁ gaseous species, meteorological parameters and tracers during haze and clean periods; (c) comparison of the averaged absolute concentrations of the PM₁ species, gaseous pollutants, meteorological parameters, ratios and combustion tracers during the haze (solid) and clean periods (pattern).



995

1000

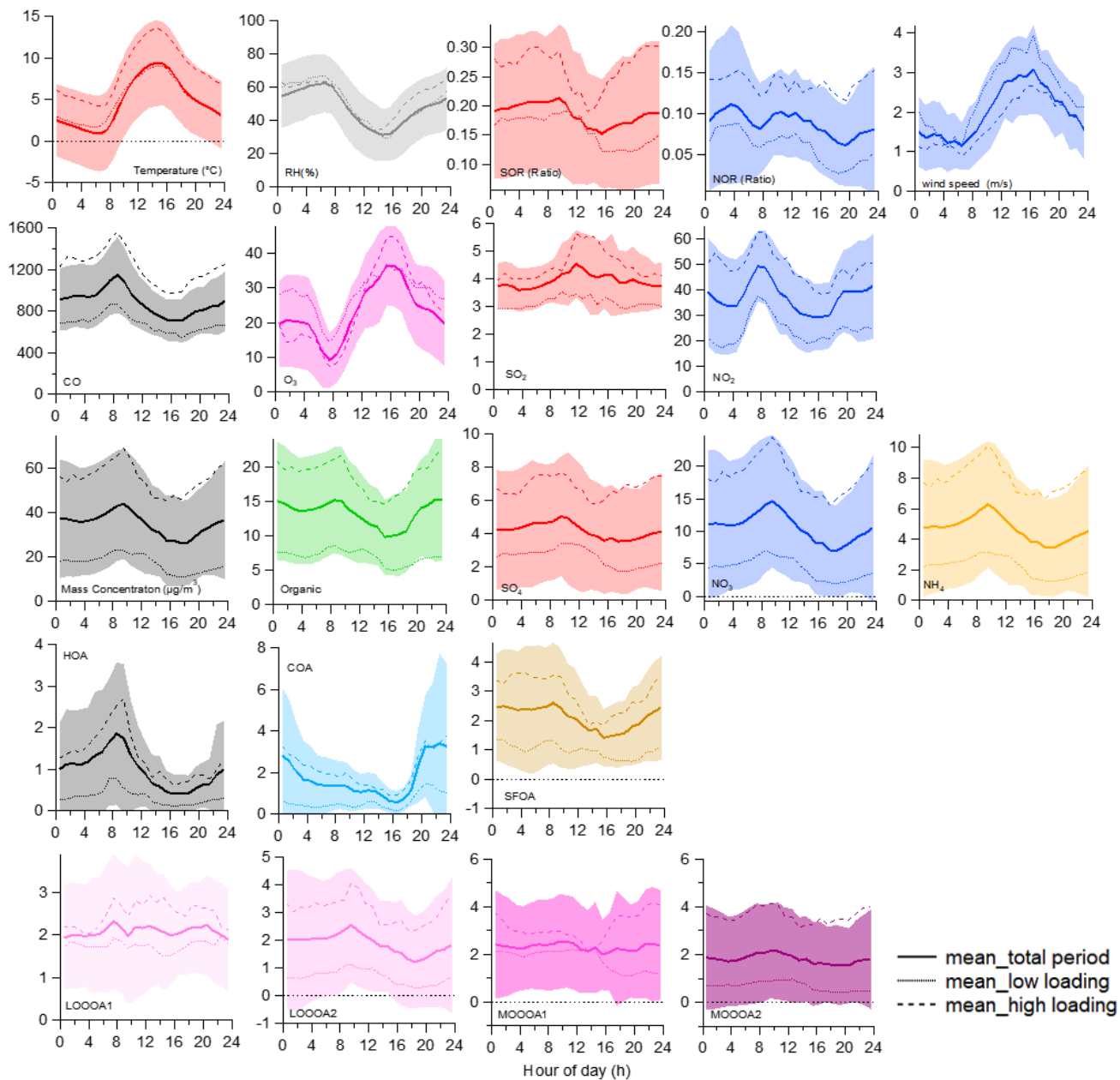
Figure 5: Overview of the chemical composition of the submicron aerosols at the Korea Institute of Science and Technology (KIST) in the SMA and Beijing from February 28, 2019, to March 16, 2019, including two haze episodes: (a) time series of the wind direction (WD), with the colors showing the different wind speeds (WSs) in the SMA; (b) time series of PM₁+BC in the SMA and of PM₁ in Beijing; (c) time series of ammonium (NH₄⁺) in the SMA and Beijing; (d) time series of sulfate (SO₄) in the SMA and Beijing; (e) time series of nitrate (NO₃⁻) in the SMA and Beijing; (f) time series of the organic and stacked contributions of the sources of the OA in the SMA and Beijing. Note that the time series of each species in Beijing is modified to KST based on Beijing Time.



1005

1010

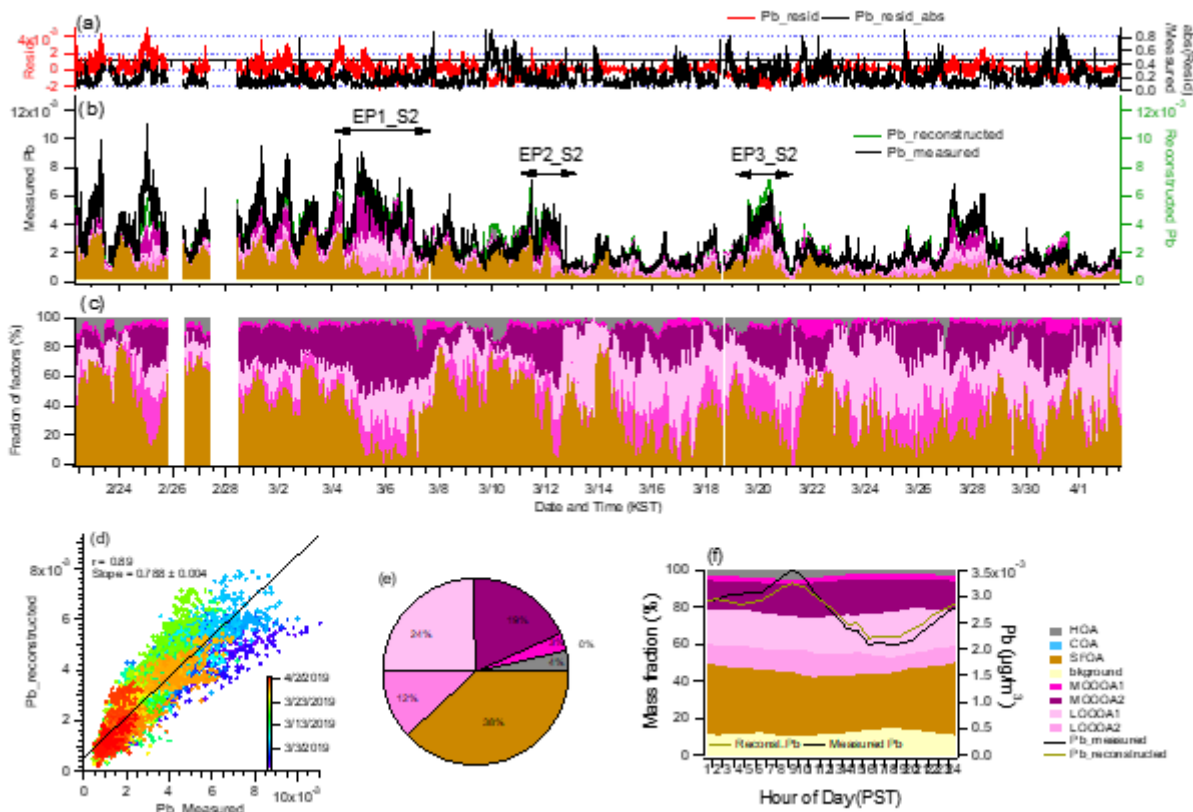
Figure 6: Overview of the chemical composition of the submicron aerosols at the Korea Institute of Science and Technology (KIST) in the SMA and Beijing from March 18, 2019, to March 23, 2019, including one haze episode: (a) time series of the wind direction (WD), with the colors showing the different wind speeds (WSs) in the SMA; (b) time series of PM₁+BC in the SMA and of PM₁ in Beijing; (c) time series of ammonium (NH₄⁺) in the SMA and Beijing; (d) time series of sulfate (SO₄) in the SMA and Beijing; (e) time series of nitrate (NO₃⁻) in the SMA and Beijing; (f) time series of the organic and stacked contributions of the sources of the OA in the SMA and Beijing. Note that the time series of each species in Beijing is modified to KST from Beijing Time.



1015

Figure 7: Comparison of the one-hour averaged diurnal profiles for the various meteorological parameters (top row), gas-phase species (second row from the top), PM₁ species (third row), primary OA (fourth row) and secondary OA (fifth row) between the high- (haze) and low-loading (clean) periods. The solid line and shaded area indicate the mean ± SD. The dotted line indicates the low- (clean period) and high-loading periods (haze period).

1020



1025

Figure 8: Diagnostic plots of the Pb decomposition results. (a) Time series of the ratio of the residual to the measured Pb concentration and variations in the absolute fitting residuals; **(b)** time series of the measured Pb and the stacked contributions of all fitted sources of the OA; **(c)** time series of the contributions of all fitted sources of the OA; **(d)** scatter plot and linear fit between the measured and reconstructed Pb concentrations where a good agreement was observed between the measured and reconstructed Pb concentrations, with a linear regression slope of 0.79 and r value of 0.89.; **(e)** the average contribution of the different components to Pb; **(f)** diurnal cycles of the contribution of the different sources of the OA and the reconstructed and measured total Pb mass concentrations